Volumetric Additive Manufacturing of Embedded Channels for Studying Flow and Permeation in Hydrogel Systems

Julia Stanny[a,b], Agathe Thiry[b, c], Ilargi Balda Lorenzo[a, d], Adam Junka [e], Kacper Pietrzak [e], Marco De Corato[f], Maria Jose Gomez-Benito[f], Eleanor Stride[b], Armin Shavandi[a]*

[a] Université libre de Bruxelles (ULB), École Polytechnique de Bruxelles, 3BIO-BioMatter, Avenue F.D. Roosevelt, 50 - CP 165/61, 1050 Brussels, Belgium

[b] Institute of Biomedical Engineering, Botnar Research Centre, University of Oxford, Windmill Road, Oxford, OX3 7LD, United Kingdom

[c] Ecole européenne d'ingénieur en génie des matériaux (EEIGM), Université de Lorraine, 6 rue Bastien-Lepage, 54000, Nancy, France

[d] Universitat de Barcelona, Facultad de Física, Carrer de Martí i Franquès, 1, 11, Distrito de Les Corts, 08028 Barcelona, España

[e] P.U.M.A., Platform for Unique Model Application, Department of Pharmaceutical Microbiology and Parasitology, Wroclaw Medical University, Borowska 211a, 50-556 Wroclaw, Poland

[f] Aragon Institute of Engineering Research, University of Zaragoza, Zaragoza 50018, Spain

* *Corresponding author Armin Shavandi (armin.shavandi@ulb.be)* and *Julia Stanny (julia.siminskastanny@ulb.be)*

Abstract

Creating perfusable vascular networks that replicate physiological flow remains a major challenge in tissue engineering. We present a rapid (<1 min) volumetric additive manufacturing (VAM) method for fabricating tunable, biologically relevant vascular structures that support controlled perfusion. A recyclable GelMA/PEGDA resin was optimized to produce high-fidelity hydrogels with embedded channels. To study how flow, structure, and function interact, we designed modular perfusion platforms providing precise control over physiological shear stress (3–50 dyne/cm^2), flow rates (1–15 mL/min), and pulsatile or continuous flow. These systems enable endothelial attachment, stable perfusion, and permeability measurements, supporting physiologically relevant flow and mass-transport studies for vascularized grafts and drug-delivery assays. In addition to controlled perfusion, the VAM process allows fast prototyping (<45 s) and improved biomimicry by generating vascular architectures within soft-tissue–like hydrogels (~10–12 kPa). The platform also permits independent pressure modulation inside the vessel and surrounding matrix, with simulations closely reflecting experimental flow and permeability data and confirming diffusion-dominated transport. Together, this framework provides a versatile resource for translational vascular modeling and drug-delivery research.

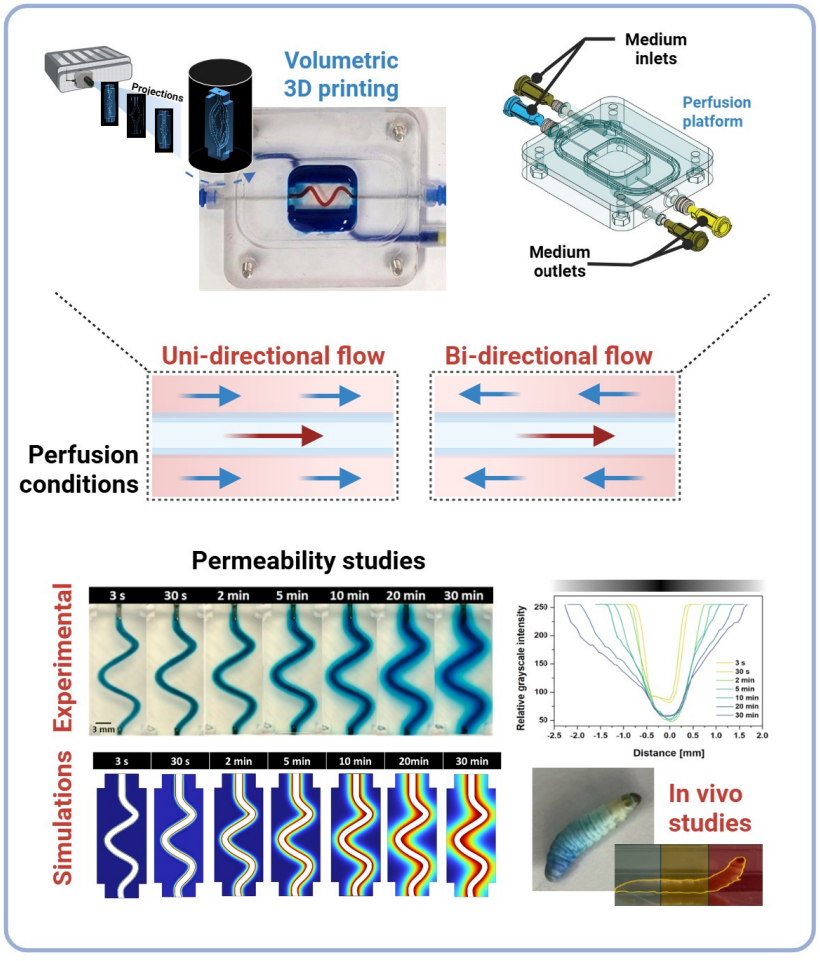

Keywords: volumetric printing; volumetric additive manufacturing; perfusion; permeation; vascular tissue engineering; simulations; vessel wall shear stress.

1. Introduction

Biofabrication techniques have transformed tissue engineering by enabling precise control over the 3D arrangement of cells and biomaterials [1]. However, recreating vascular networks remains a crucial aspect of successful tissue engineering, and it remains a significant challenge [2, 3].

Static culture conditions are insufficient to recapitulate the dynamic environment of living tissues [4]. To date, most perfusable vascular models are confined to microfluidic channels [5], which are commonly categorized as organ-on-chip platforms [6, 7]. These systems are primarily fabricated using lithography techniques, including polydimethylsiloxane (PDMS) molding, to create channels that serve as substrates for cell culture. While these platforms approximate some physiological dynamics, their reliance on rigid structures and small geometries limits their broader applicability in tissue engineering. Hydrogels are increasingly employed in vascular models, providing a more physiologically relevant 3D environment than PDMS that supports the seeding of endothelial cells (ECs) and the formation of vascular networks through vasculogenesis [6, 8]. Although these networks enable the study of barrier function, their randomly oriented geometries limit flow studies or define wall shear stresses [6, 9]. In some cases, channels are created within PDMS and then coated or shaped within hydrogels [10, 11]. For example, vascular geometries can be fabricated by casting a hydrogel around a steel needle, where the lumen is formed upon removal of the needle. However, this approach is limited to creating straight channel geometries [10] with the channel size determined by the needle diameter, typically 60-300 µm [12, 13]. Although organ-on-chip platforms aim to replicate native dynamic conditions, they often require multiple components and involve a cumbersome assembly process [14]. To address the limitations of existing vascular models, researchers have used 3D printing techniques [15, 16]. Significant efforts have been made to fabricate vascular structures using extrusion bioprinting [17], sacrificial embedded printing [18], melt electrowriting [19], digital light processing (DLP) [20, 21], and hybrid approaches [15, 22, 23]. While these methods have achieved more complex channel geometries than simple tubes, the lengthy fabrication time and difficulties in assembling fluid-circulating setups remain major drawbacks. Volumetric additive manufacturing (VAM) is a promising approach to vascular printing that can rapidly sculpt photoresponsive hydrogels into complex 3D structures, including channeled geometries [24-26], within approximately one minute [1, 27].

Among VAM resins for bio applications, gelatin has emerged as a leading material, due to its favorable thermal gelation and ease of modification [23, 28, 29]. However, gelatin alone often fails to produce mechanically robust constructs capable of maintaining their shape [30]. Polyethylene glycol diacrylate (PEGDA), though limited by its low viscosity (~120 cP), complements gelatin by enhancing mechanical stability when used in combination [31]. Although recent literature reports the use of gelatin–PEGDA resin systems [32], the reusability of these materials for subsequent volumetric printing cycles has not received much attention.

Similarly, whilst VAM solves numerous challenges in current vascular tissue biofabrication, a substantial portion of research in this field focuses on material exploration and printing process refinement. Successful fabrication of channel structures has been demonstrated, but the development of systems with highly controllable perfusion remains underexplored [1, 19, 33]. Using flow platforms to dynamize cell cultures within hydrogels can provide insights into how ECs sense molecular cues and regulate cell-cell adhesions, modulating gas, ion, and other transports [34, 35]. Additionally, such platforms can be utilized in the future to study flow-driven morphological changes in EC alignment, enhancements of adhesion bonds, cell-cell junctions, or cytoskeletal developments, using appropriate immunofluorescent staining [10, 36].

From a model validity standpoint, within the same vessel, shear stress levels and flow profiles can vary significantly due to geometric features, including vessel branches and curvature [37]. Recapitulating these particularities has not been possible using wire-templating or extrusion printing techniques. Models capable of reproducing physiological shear stress profiles are therefore essential for studying mechanobiological disease mechanisms and evaluating therapeutic strategies.

In this work, we present a novel strategy to introduce controlled flow dynamics, as previously achieved for microfluidic PDMS vascular models, but this time integrating flow constraints with structures fabricated through VAM methods. Previous studies have employed GelMA–PEGDA in VAM [38], demonstrating high print fidelity but without optimization for resin reusability or integration with modular perfusion platforms. In contrast, our work systematically optimizes optical/mechanical balance, evaluates photoinitiator toxicity trade-offs, and introduces reusability testing for sustainability.

To replicate physiological conditions, we develop an *in vitro* platform for dynamic perfusion. This system is designed to simulate physiological shear stresses and flow rates, supporting a range of fluid-handling configurations, including syringe pumps, peristaltic systems, and rocker platforms. The proposed platform offers a valuable tool for investigating vascular biology, drug delivery, and the development of clinically relevant *in vitro* models.

2. Results and discussion

2.1 Biomaterial resin formulation and VAM

Hydrogels composed of GelMA and PEGDA have been widely used in extrusion-based bioprinting [39, 40] ; however, their adaptation to VAM requires optimization. In multi-component systems, differences in optical clarity, viscosity, and polymerization kinetics between components can lead to uneven crosslinking or loss of resolution during volumetric exposure. While several studies have successfully printed multi-material resins via VAM [33, 41], each formulation requires tailored adjustments of printing parameters to accommodate the specific physicochemical interactions between its components.

In VAM, thermally solidified GelMA can hold the print through multiple rotation sequences when 2D images are projected to cure the material selectively [42] (**Figure 1A**). GelMA was selected as the base material due to its biocompatibility, enzyme-mediated biodegradability, and thermo-reversible properties, which facilitate structural integrity during bioprinting [24]. Polyethylene glycol diacrylate (PEGDA) was added to enhance mechanical stability and print fidelity [30]. Nine resin formulations were prepared, varying GelMA (5%, 10% w/v) and PEGDA (5%, 10% v/v) concentrations, along with lithium phenyl(2,4,6-trimethylbenzoyl)phosphinate (LAP) photoinitiator (0.3, 0.5, 1.0 mg/mL), (**Supplementary information (SI), Table S1 –** Formulation of biomaterial resins), based on the previous studies exploring GelMA printability [23, 28, 29].

The optimal light dose was selected based on quantitative metrics, including the dimensional accuracy of disc-shaped structures [29, 43] measured via coherence-contrast microscopy and benchmark geometries such as a chess figure (**Figure 1C-E**, **SI, Figure S1**). Based on a comparative evaluation, we identified 370 mJ/cm² as the optimal dose for the GelMA 5% + PEGDA 10% + LAP 0.3 mg/mL formulation. This dose provided the best balance between print fidelity and mechanical robustness. At 350 mJ/cm², the constructs exhibited insufficient curing, resulting in deformation and poor feature resolution. At 400 mJ/cm², over-polymerization effects, such as blurred

features and reduced translucency, were observed. The 370 mJ/cm² dose produced stable, self-standing structures with a resolved geometry, as confirmed by coherence-contrast microscopy and photorheology.

The results indicated that increasing the PEGDA concentration improved structural stability and resolution [43], as demonstrated by constructs printed with 10% PEGDA and 5% GelMA; however, increasing PEGDA content shifts the resin composition further from native ECM biochemistry, a limitation to be addressed in future ECM-enriched formulations.

Formulations containing higher GelMA concentrations (10%) resulted in increased resin turbidity, likely due to enhanced molecular aggregation and light scattering, which reduced printing resolution and led to fragile, difficult-to-retrieve objects. Conversely, lowering GelMA to 5% while increasing PEGDA to 10% improved structural stability and transparency (**SI, Figure S1**).

We also varied the LAP photoinitiator concentration (0.3–1 mg/mL) to determine the minimum amount required for successful printing while maintaining resolution and potentially reducing cytotoxicity. Photorheology tests showed that the formulation with the lower LAP concentration (0.3 mg/mL) exhibited slower, more controlled polymerization kinetics (peak modulus reached in ~30 s), allowing gradual curing that minimized overcuring and increased printing accuracy.

In contrast, for our specific formulation and standard dose settings, higher LAP concentrations (1 mg/mL) resulted in faster polymerization (~10 s), which, without dose re-optimization, led to reduced feature definition and signs of overcuring (**Figure S1**). Other studies have successfully employed 1 mg/mL LAP in VAM [23, 33]. Our observations should thus be interpreted as formulation and dose-specific, rather than as a general limitation of high LAP concentrations. Photorheology (**Figure 1B**) further indicates the importance of controlled polymerization, especially in chain growth systems such as GelMA and PEGDA [24, 28]. Following the dose experiments, the 5% GelMA + 10% PEGDA + 0.3 mg/mL LAP combination was selected for its balance of mechanical stability, optical clarity, and reduced LAP content to improve cell compatibility.

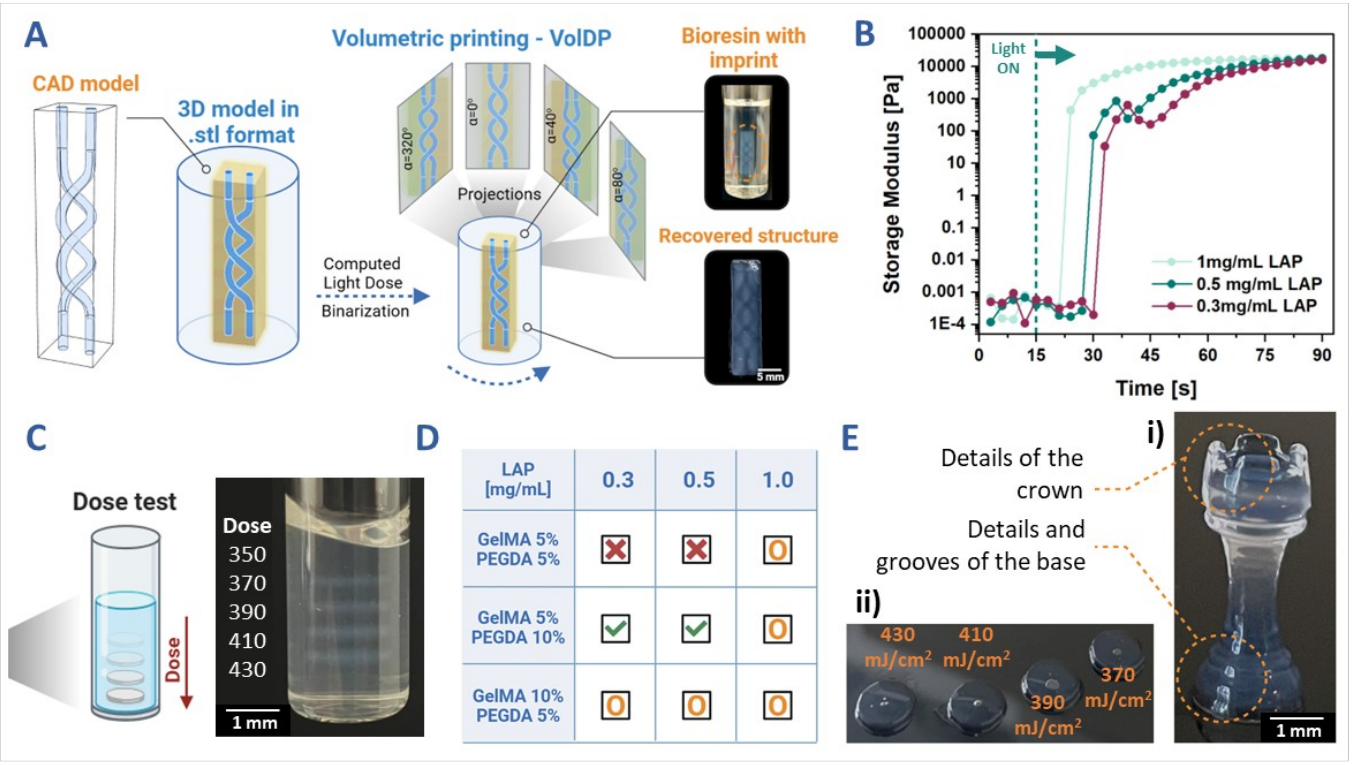

Figure 1 A) *Schematic of VAM of double-spiral channeled geometry, with the imprinted geometry and the recovered construct;* ***B)*** *Time-sweep test showing the photocrosslinking pattern for variously formulated bioresins, the dashed line represents the moment from which the 405 nm light was on, representative plots, n=3;* ***C)*** *Schematic of the light dose optimization for resins at different light doses, performed dose test is used to determine the light exposition of the material required to photocrosslink the projected patterns with an example of the test used to adjust the dose for GelMA 5% PEGDA 10% biomaterial resin;* ***D)*** *Volumetric printability results for various bioresins with different LAP content (derived based on the results from Figure S1). The green tick indicates high-detail printability, the orange circle denotes printability with compromised detail and reduced stability, and the red 'x' marks poorly printable samples, in which the disc structures were not distinguishable.* ***E)*** *VAM results for GelMA 5% PEGDA 10% LAP 0.3 mg/mL biomaterial resin (i) disks printed with different light doses and (ii) chess figure revealing the structural details of the print.*

2.2 Biomaterial-Resin Transparency and Print Resolution

The effectiveness of VAM relies on materials having high optical transparency and minimal light scattering or absorption [44, 45]. To crosslink the resin, light must pass through the entire build volume without distortion or attenuation, making resin transparency and the photoinitiator concentration crucial [25].

We compared our resin to GelMA (10% with 1 mg/mL LAP), which is commonly used in VAM. A lower GelMA concentration control (e.g., 5% GelMA with 0.3 mg/mL LAP) was not included, as formulations below 10% GelMA did not yield stable structures under our VAM conditions, making them unsuitable for meaningful comparison. Prints of a channeled object showed uneven edges and over-polymerization in GelMA, while resin produced precise striations, typical of VAM, confirming its precision curing (**Figure 2B**).

Lower absorbance of the resin at 405 nm (24.17 ± 0.22%) compared to pure GelMA (28.60 ± 0.06%) indicates reduced attenuation of curing light, directly translating to higher curing precision for the resin. Measurements at 600 nm, although not directly related to the curing wavelength, support the overall superior transparency and lower optical scattering , thereby enhancing overall print precision (**Figure 2C, SI Table S2**). A greater refractive

index contrast was observed between the uncured resin and its corresponding hydrogel (~0.06%) compared to GelMA, which contributed to the enhanced visibility of the resin-printed structures during the VAM curing process (**Figure 2A, 2D**, **SI, Figure S2-C**). The high turbidity in GelMA and resins with higher GelMA content (**SI, Figure S1)** is likely due to greater heterogeneity within the resin matrix, possibly involving the formation of larger polymer aggregates, resulting in increased light scattering and reduced precision in light-guided curing (**Figure 2D**) [44]. We hypothesize that the compatibility of GelMA and PEGDA for high-resolution multimaterial VAM can be attributed to their similar light doses for polymerization, comparable photocrosslinking patterns (**SI, Figure S2-A**), and closely matched refractive index values [47] prior to crosslinking (**SI, Figure S2-C**).

Although previous studies report that polymerizing 5% (w/v) GelMA with 0.1% (w/v) LAP requires ~250 mJ/cm² [1], and PEGDA hydrogels require ~236 ± 14 mJ/cm², these values serve only as reference points. In our resin formulation, the polymerization behavior reflects a new composite system, where the optimal dose depends on the individual polymer thresholds and concentration, molecular weight, degree of functionalization, and the non-orthogonal interaction between GelMA and PEGDA radical polymerizations. Therefore, empirical optimization of the light dose was essential to ensure proper crosslinking, and the final dose (370 mJ/cm²) was selected based on print fidelity and mechanical integrity. It is worth noting that, incorporating native ECM components could increase light-dose requirements due to added scattering and may soften the network, affecting mechanical properties and printing resolution [46].

Adjusting the light dose and avoiding overexposure, we could print precise structures with embedded perfusable channels (**Figure 2E**). Coherence contrast microscopic analysis was performed post-3D printing to evaluate the maximum resolution of the VAM models. Two geometries were printed, emphasizing either positive or negative features (**Figures F-i and G-i**). The minimum thickness of quadrangle tapering was 49 ± 7 µm for horizontal prints and 43 ± 4 µm for vertical prints. The achieved resolution limits (approximately 40–50 µm) closely matched the model dimensions, confirming the high printability and resolution of both the material and VAM method. This resolution is sufficient for modeling intermediate microvascular structures with meaningful biological relevance.

A clear distinction was observed between the printable and non-printable diameters (**Figure 2G, iii and iv**). The design remained successfully printable until the channel diameter reached 186 ± 28 µm, beyond which perfusability was compromised (**Figure 2G-iii**), establishing the resolution limit for negative concave features at ~200 µm. While this resolution enables the modeling of intermediate-sized vessels, such as arterioles and venules, it is insufficient to replicate physiological capillary networks, which typically range in diameter from 5 to 10 µm.

The light intensity patterns simulated using the printer software (Apparite®) enabled predictions of potential over-curing areas and minimal printable diameters (**Figure 2F-iii, G-iv**). This facilitated iterative adjustment to the design constraints to achieve perfusable structures.

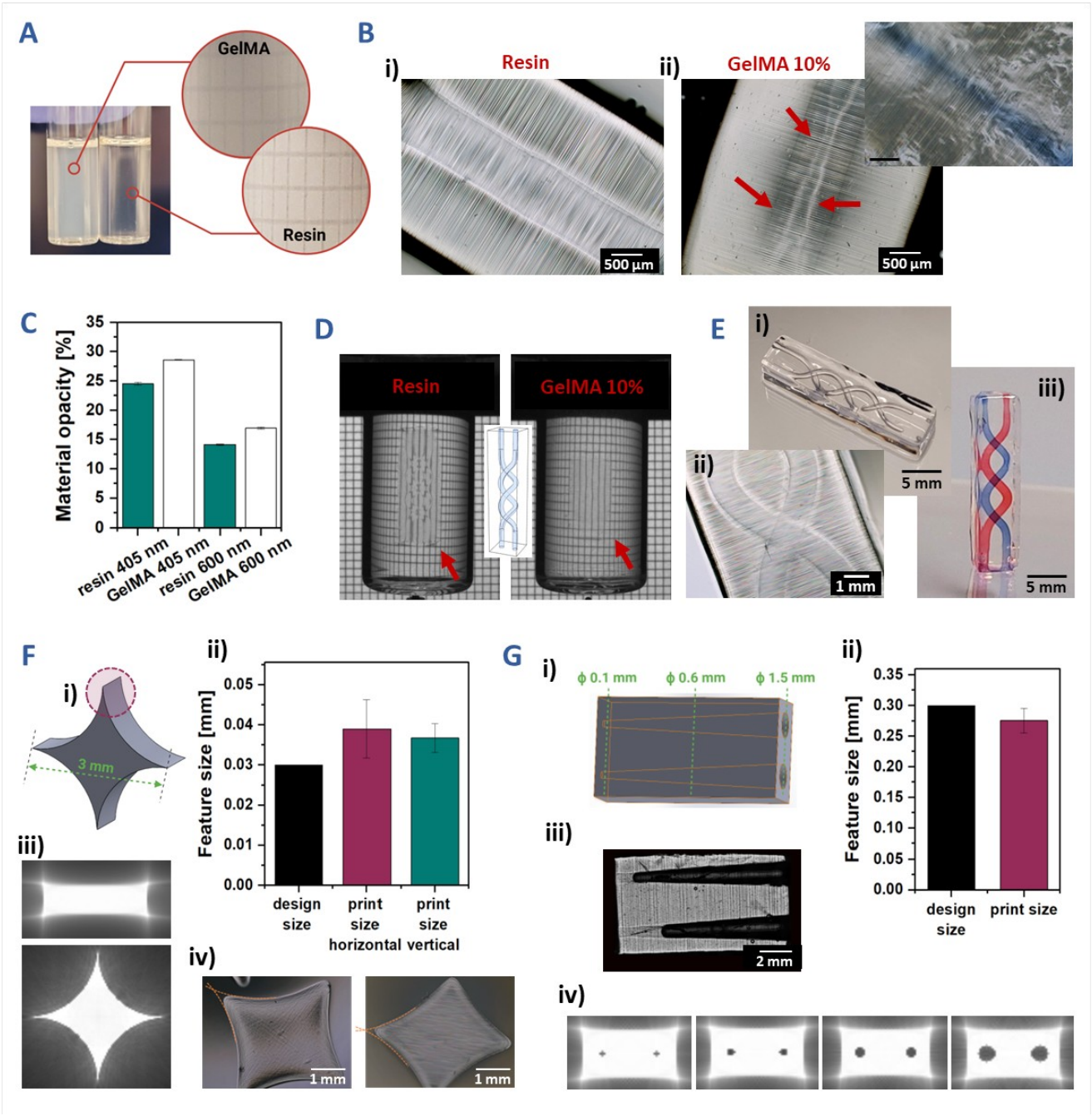

Figure 2 A) *Photographs of the GelMA and resins when loaded to the printing vials, the grid behind the vial is less visible for GelMA resin;* ***B)*** *VAM of resin showed sharper and clearer internal channels compared to GelMA;* ***C)*** *Material opacity results obtained based on absorbance measurements for GelMA and both resin and hydrogel at 405 nm and 600 nm, n=3, mean ± SD., differences between groups were significant at p ≤ 0.001, two-way ANOVA with Tukey post-hoc test;* ***D)*** *Images of the vials after VAM of double-channeled structure, the object is better visible for resin than for GelMA likely due to a higher differences in refractive indexes between the resin and hydrogel formed due to photocrosslinking;* ***E)*** *Images of the VAM double-channel structure, emphasizing on the structural details (ii) and perfusability of the channels (i, iii);* ***F)*** *VAM results of the highest-resolution positive features (circular marking) (i) shows the designed model, (ii) comparison of the printed feature size with the model size, n=3, mean ± SD., data were not significant at p > 0.05, Kruskal-Wallis with Dunn-Sidak post-hoc test; (iii) software-generated light projection patterns, corresponding to the design, (iv) VAM structures used for evaluation* ***G)*** *VAM results of the highest-resolution negative features (i) shows the designed model, (ii) comparison of the printed feature*

size with the model size, n=3, mean ± SD., data were not significant at p > 0.05, Kruskal-Wallis with Dunn-Sidak post-hoc test; (iii) VAM structures used for evaluation, (iv) software-generated light projection patterns, corresponding to the design.

2.3 Bioresin Stability, Reusability and Rheological Properties

During the VAM printing, a semi-solid gelatin network helps stabilize PEGDA monomers, preventing the forming structure from settling during light exposure and rotation. When cooled below 25℃, GelMA physically crosslinks through hydrogen bonding, which increases the storage modulus (G'). The resin shows a similarly high G' (≥ 100 Pa) at temperatures below 30℃ (**Figure 3A-i**). As the temperature rises to about 30℃, G' sharply decreases, indicating a reversible gel-sol transition where viscous behavior starts to dominate (flow point) [47]. Beyond this point, the material softens (G' < 0.001 Pa) and flows freely. The precise transition temperature depends on the concentration of GelMA and the degree of methacrylation [48, 49]. This reversible thermal transition is beneficial for VAM, enabling easy recovery of the printed construct once the surrounding material liquefies (**Figure 3A-ii**).

During VAM, the entire hydrogel volume is exposed to light, resulting in an anisotropic 3D dose distribution throughout the resin. Unpolymerized resin can be recovered and reused (**Figure 3B**), but prior exposure may lead to unwanted partial grafting. Repeated light exposure can gradually alter the resin's crosslinking behavior. Rheological analysis across eight consecutive printing cycles (**Figure 3C**) showed a steady increase in curing time, from 15 seconds in the first print to about 27 seconds in the eighth. This slower curing is likely caused by radical depletion or cleavage of the photoinitiator after repeated light exposure [31]. Oxidative degradation of the polymer network, enhanced by exposure to atmospheric oxygen during handling, may also reduce crosslinking efficiency and mechanical strength [50]. After the first three prints, the maximum G' values after 110 s of exposure decreased by 5-8%, but remained stable, indicating consistent performance in these cycles (**Figure 3E**). From the fourth cycle onwards, G' declined more rapidly, reaching a reduction of about 45 % by the eighth print (~1400 Pa difference compared to the first cycle). This loss in G’ likely reflects both photoinitiator depletion and chemical changes accumulating in the resin with repeated use. Thermal effects were ruled out, as heating and cooling cycles showed no influence on the resin’s photocrosslinking behavior (**SI, Figure S2-B**).

A comprehensive mechanical characterization of the GelMA–PEGDA resin, including indentation testing, Young’s modulus measurement, and viscoelastic analysis, was previously reported in our recent work [51]. In that study, GelMA–PEGDA hydrogels showed a higher Young’s modulus (≈130 Pa) than GelMA alone (≈90 Pa), along with improved structural stability and reduced swelling. These values are within the lower physiological range of native vascular tissue (100–1000 Pa) [52].

Across eight consecutive printing cycles, the minimum light dose needed to print an 8 mm diameter star-shaped construct increased from 585 ± 17 to 825 ± 21 mJ/cm^2 (**Figure 3D**), consistent with the longer curing times observed (**Figure 3C**). A gradual reduction in the size and precision of the parts was also noted (**Figure 3H**), making them more fragile to handle. The areas and perimeters of the printed objects decreased by ~41% and 27%, respectively (**Figure 3G, SI Figure S2-D**). At the same time, the size of fine positive features increased two to threefold, indicating reduced printing resolution (**Figure 3F**).

The ~45% reduction in G’ after eight cycles highlights the mechanical limitations of reusing resin. This decline, coupled with slower curing and reduced structural precision, became most pronounced after the fourth cycle. Blending recovered resin with fresh material at 1:1 or 1:2 ratios partially restored performance, but variability remained. Although resin reuse reduces costs, preparation time, and waste, particularly for complex or costly formulations, it introduces inconsistency. Future work should focus on resin regeneration strategies, such as photoinitiator replenishment or oxidative stabilization, to maintain reliable performance over repeated use.

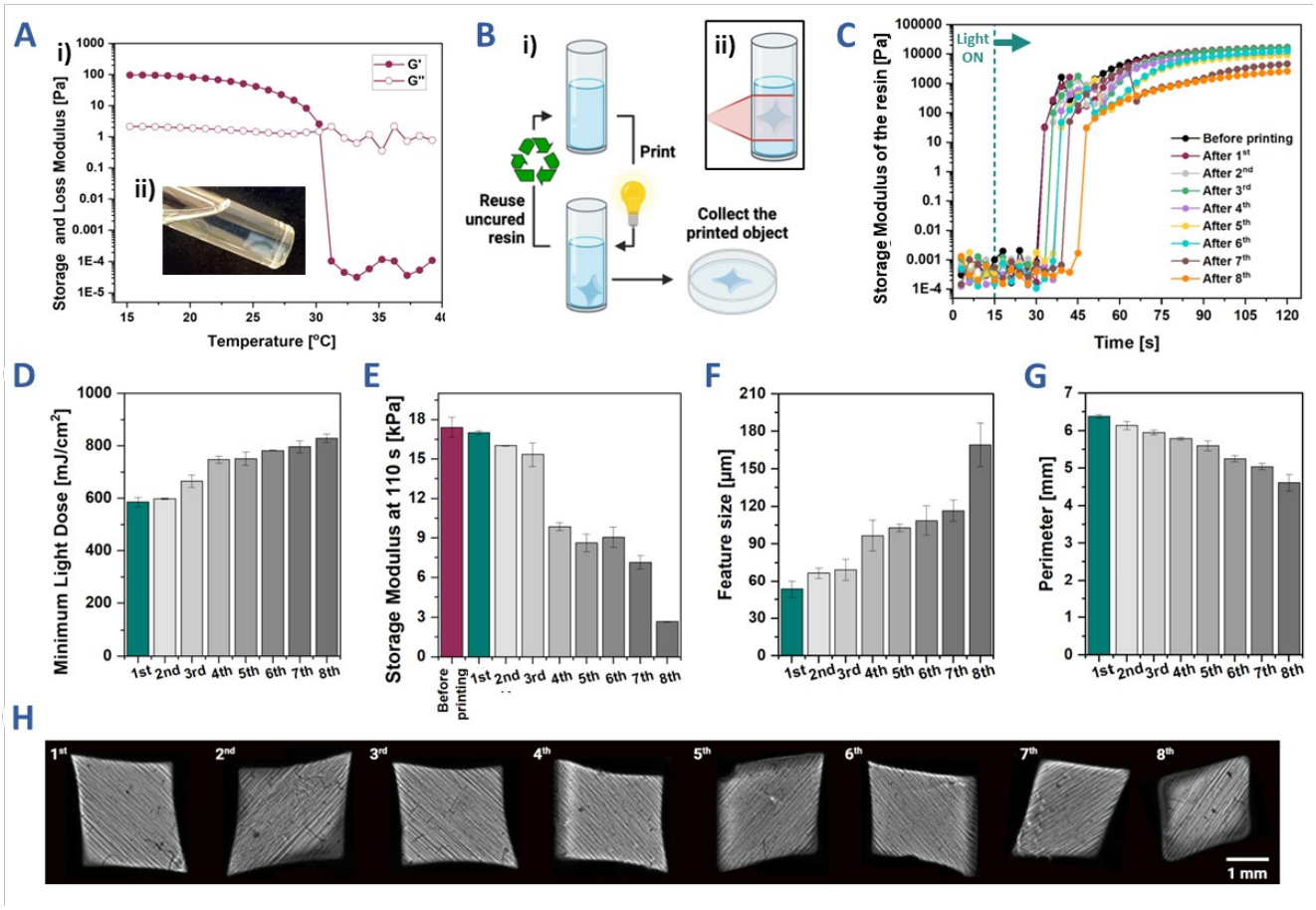

Figure 3 A) *Temperature sweep test for resin – (i) (representative plot based on n=3) and (ii) VAM shape remaining solid once the rest of the resin is liquified;* ***B)*** *Schematic illustration of the resin reusability concept, where the unpolymerized resin is recovered and used for subsequent prints (i), (ii) – exposure of the material volume during object printing;* ***C)*** *Photorheology tests for resin after every VAM cycle (representative plots based on n=3), the dashed line represents the moment from which the 405 nm light was on;* ***D)*** *Minimum light dose required to crosslink the resin after repeated printing n=3, mean ± SD., results were significant at p ≤ 0.05 for 1st vs. 8th print and 2nd vs. 8th print, Kruskal-Wallis;* ***E)*** *Storage Modulus values at 110 s of the resins used for consecutive printing, n=3, mean ± SD., results were significant at p ≤ 0.05 for before printing vs. 8th print and 1st vs. 8th, Kruskal-Wallis;* ***F)*** *Resolution of the printed samples positive features after consecutive printing n≥3, mean ± SD., results were significant at p ≤ 0.05 for 1st vs. 8th print, Kruskal-Wallis;* ***H)*** *VAM objects obtained from the reused resin, the numbers correspond to the print count.* ***G)*** *Perimeter of the VAM design after consecutive printing, n=3, mean ± SD., results were significant at p ≤ 0.05 only for 1st vs. 8th print, Kruskal-Wallis;*

2.4 Biocompatibility of the Photocrosslinked Hydrogel Constructs

The biocompatibility of the hydrogel resin was evaluated by assessing EA.hy926 cell attachment and viability. Cell suspensions were added to the wells containing hydrogel discs at the bottom (**Figure 4A**). Initially, only a few cells were observed on the surface, but the cells gradually aggregated and spread across the discs' surface (**Figure 4B-C**).

For microscopic comparison of cell attachment with standard culture conditions on well-established tissue culture substrates such as GelMA, we refer to our parallel study [51], in which cells cultured on GelMA and GelMA–PEGDA hydrogels exhibited comparable attachment and growth, confirming the suitability of the material for cell culture [51].

Colorimetric viability assays further confirmed that the photocrosslinked hydrogel discs supported cell survival with consistently high viability (>80%) maintained from day 1 to day 7 (**Figure 4D**). For quantitative assessment, EA.hy926 cells were seeded on 2D hydrogel discs (diameter 5 mm, thickness 0.6 mm) fabricated from the optimized GelMA–PEGDA resin. viability was monitored for seven days using the CellTiter 96® Aqueous One Solution (MTS) assay with day 1 values normalized to 100%. Increased absorbance over time indicated proliferation (**Figure 4D**). The MTS assay was selected for its compatibility with adherent cells; potential optical interference from the hydrogel was minimized by using thin discs (≤1 mm) and removing media before absorbance measurements. Fluorescent z-stack imaging showed distinct cell morphologies at different focal planes. Cells at the bottom exhibited elongated morphologies, indicative of robust integrin-mediated adhesion facilitated by gelatin-derived bioactive peptides (**Figure 4E-iii**) [53]. In contrast, cells in the upper layer appear more rounded (**Figure 4E-i, ii**), likely due to reduced substrate contact and therefore limited availability of adhesion cues.

Consistent with previous studies, cells adhered and proliferated better in GelMA-PEGDA hydrogels than in PEG-only systems [54]. Additionally, in our previous work we have also evaluated the printed models with HUVECs and osteosarcoma cell lines [51], showing cell lining created with VAM imprinted channels.

Used in this study, EA.hy926 endothelial-like cells adhered to the inner surfaces of the printed channels and remained viable over time (**Figures 4F-G).** Full circumferential endothelialization, however, was not assessed here. Confirming complete lumen coverage requires confocal cross-sections or volumetric imaging. In this study, EA.hy926 cells were not encapsulated within the VAM constructs as the GelMA–PEGDA (5%/10%) formulation was optimized primarily for print resolution and mechanical stability, rather than cytocompatibility during photopolymerization.

EA.hy926 cells, a hybrid endothelial cell line derived from HUVECs and A549 carcinoma cells, were chosen for their robustness and reproducibility, but do not fully replicate the phenotype or functional responses of primary endothelial cells. Thus, these experiments serve as a proof of concept demonstrating the basic cytocompatibility and perfusion compatibility of the printed constructs, providing a foundation for future studies using primary endothelial or co-culture systems.

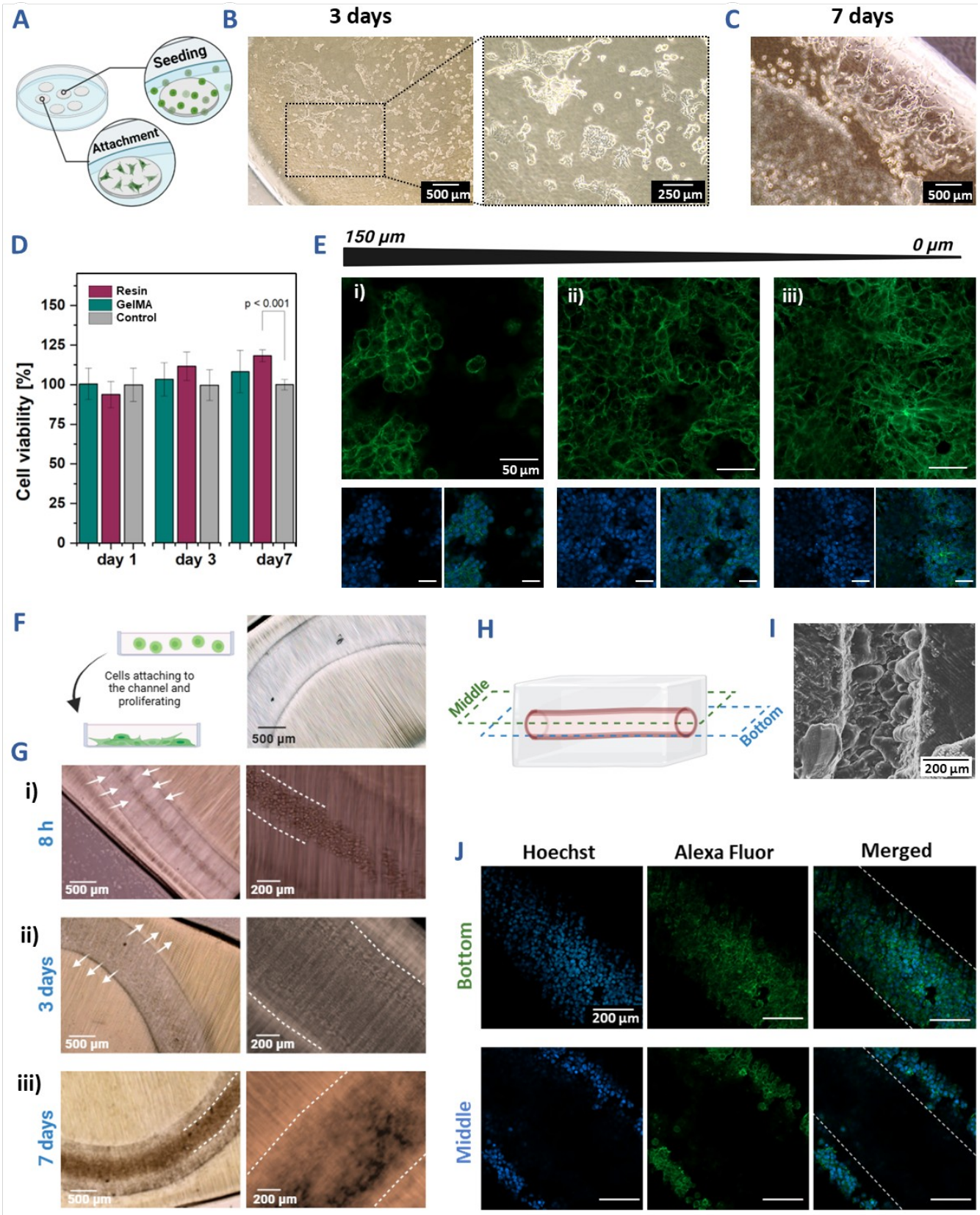

Figure 4 A) *Schematic depicting cell seeding onto hydrogel discs; Microscopic photos of the hydrogel surface with attached EA.hy926 cells after* ***B)*** *3 days and after* ***C)*** *7 days of culture;* ***D)*** *Cell viability after 1, 3 and 7 days, n=8, mean ± SD., $p < 0.05$, one-way ANOVA with Dunn-Sidak post-hoc test;* ***E)*** *Z-stack images (i-iii) of the EA.hy926 cells attached and growing on the*

surface of hydrogel discs, cell nuclei are labelled in blue and F-actin in green, scale bars correspond to 50 µm, ***F)*** *Schematics of the EA.hy926 cells settling at the channel's bottom and the image of VAM channel prior to cell seeding;* ***G)*** *VAM channel with seeded EA.hy926 cells (i) after 8h of incubation, (ii) after 3 days, EA.hy926 cells are more dispersed and uniformly covering the lumen, (iii) after 7 days, EA.hy926 cells start to accumulate at the bottom of the channel;* ***H)*** *Schematic of the VAM vascular model showing the middle and bottom layer of the channel at which the imaging was performed;* ***I)*** *SEM image of the sample crossection revealing the channel;* ***J)*** *Images of the fluorescently labelled EA.hy926 cells (day 7) lining the VAM channel, image taken in the middle of the structure reveals presence of EA.hy926 cells on the walls, shaping the lumen.*

Volumetrically printed networks were seeded with EA.hy926 cells (**Figure 4F, SI, Figure S3**). After 8 h, most injected cells had sedimented at the bottom of the channels (**Figure 4G-i**). Rotating or flipping the constructs within the first few hours post-seeding improved initial cell distribution [10]. To facilitate microscopic observations, stained samples were cut in half as depicted in **Figure 4H-I**. After 3 days, cells exhibited apparent spreading and migrating from the bottom toward the channel walls, making the basal layer less distinct (**Figure 4G-ii**). Consistent with previous findings in fibronectin-treated PDMS channels [10]. After 7 days, cells began to accumulate again along the lower surfaces, likely due to increasing density and gravitational effects.

The uneven cell distribution likely resulted from local variations in wall shear stress and flow velocity, particularly in branched regions where recirculation or low-shear zones can occur. This hydrodynamic heterogeneity, combined with gravity-driven sedimentation, contributed to the non-uniform cell coverage observed. Future optimization of seeding strategies, including dynamic rotation or controlled flow seeding, could help mitigate these effects and promote more uniform endothelial coverage.

Non-uniform cell coverage formed dense clusters that reduced light transmission during imaging (**Figure 4G-iii**). Confocal z-stack imaging (**Figure 4J**) confirmed cells within the channels. However, some gaps in coverage were visible; additional confocal z-stack imaging at multiple time points and orientations will be required in future work to distinguish true uncovered areas from sampling artifacts. Fluorescent staining of cell nuclei (**Figure S3**) further demonstrated colonization of branched vascular geometries.

2.5 Prototyping Vascular Structures and Perfusion Platform for 3D Printed Vascular Models

We investigated how the use of the resin to prototype branched vascular structures (**Figure 5A**) to mimic hierarchical branching patterns of physiological vasculature. Given that the resin has low gel strength, standalone vessels could not be fabricated by VAM; instead, channels were patterned within a 3D hydrogel matrix (**Figure 5A-B**). The resulting branched channels were perfusable, as shown by uniform dye filling (**Figure 5C, SI-video-S2**) and confirmed by perfusion tests, demonstrating unobstructed flow at physiologically relevant rates (~1–5 mL/min). These flow conditions correspond to shear rates ranging from 1600 s^{-1} to 100 s^{-1} within the range where blood viscosity remains nearly constant [55].

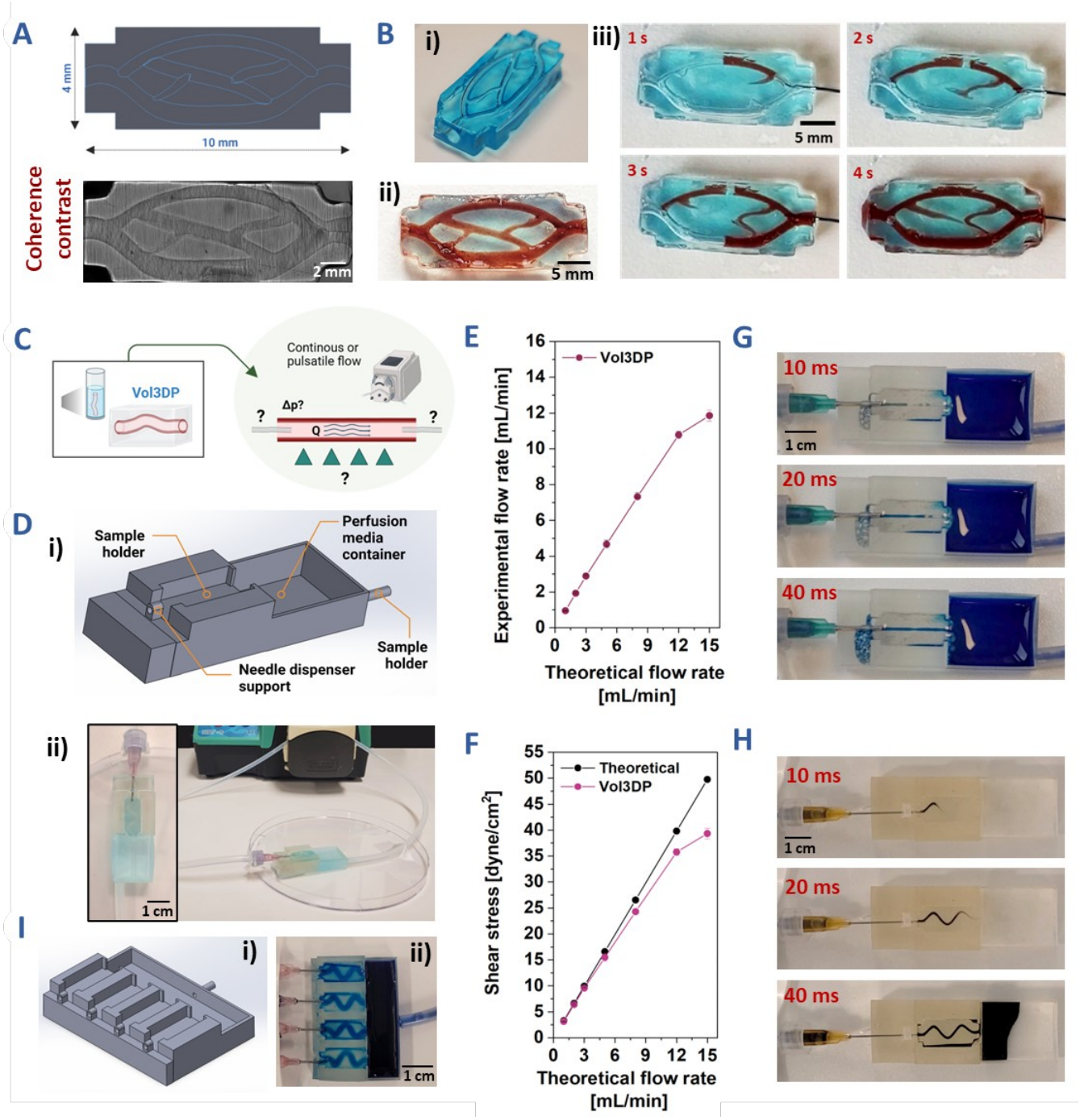

Figure 5 A) *A proof of concept design of a branched vascular network (i) and coherence contrast microscopy image of the resulting, VAM geometry (ii)* ***B)*** *Photograph of the embedded vascular patterns, after removing unpolymerized resin and filling the channels with (i) air (ii) red-colored PBS (iii) Hand-guided perfusion experiments,* ***C)*** *Schematic representation of the vascular geometries achievable within VAM (standalone channels), crucial factors to consider in designing the model-relevant perfusion platforms;* ***D)*** *The platform schematic designed for the peristaltic pump-driven perfusion of VAM channels (i). Besides, the needle holder platform is equipped with a fluid recovery container that can be directly connected to tubing, creating a closed circuit for long-term perfusion (ii) Example of the setup assembly for peristaltic pump-controlled perfusion studies for VAM models;* ***E)*** *Theoretical and experimental flow rate dependency for the VAM models* ***F)*** *The calculated shear stress values for the employed models; Examples of the perfusion studies for VAM vascular models. VAM gives higher freedom of channel geometries, easily creating straight* ***(G)*** *or sinusoidal* ***(H)*** *channels;* ***I)*** *Scaled-up platform for simultaneous perfusion of up to four VAM vascular models, (i) design schematic, (ii) assembled setup;*

3D-printed vessel models can be more complex than conventional microfluidic chips and offer a closer approximation to 3-dimensional physiological conditions [56, 57]. VAM enables fabrication of both standalone and embedded vessels, but the geometry of each construct constrains how it can be integrated into a perfusion setup. To overcome these geometry-related assembly constraints, we developed customized inlet and outlet designs for different models, provided structural support during testing, and tuned flow rates (0.5–15 mL min^{-1}) to achieve target wall shear stresses (**Figure 5C**). support platforms were designed in CAD and fabricated using Digital Light Processing (DLP) technology (**Figure 5D-i**). An example of the assembled system using a peristaltic pump is shown in **Figure 5D-ii**.

A key requirement for hydrogels used in vessel tissue engineering is their ability to withstand hydraulic pressure and maintain continuous perfusion [58, 59]. Some studies have achieved perfusion using a rocker-shaker that leverages repeated angular shifts to induce gravity-driven flow and allow multiple samples to be processed simultaneously [10]. However, such gravity-driven flow is inadequate for short channels (<4mm), where capillary forces dominate and tilting angles are limited. To address this limitation, we employed a peristaltic pump to deliver controlled hemodynamic flow (**Figure 5D-ii**), minimizing capillary effects and improving flow control within VAM vascular models.

Previous studies, including that of Bernal et al. [1], emphasized the importance of fluid-driven stimulation for biologically relevant 3D structures. However, their box-like chamber design exposed printed constructs to bulk flow without establishing a direct connection between the VAM structure and directional flow path. In our work, the development of a dedicated perfusion platform was preceded by multiple design prototypes to identify experimental challenges. Needle supports were added to ensure stable, leak-free fluid delivery. The outlet part was equipped with a fluid recovery container connected to tubing for continuous media circulation (**Figure 5D**). To increase throughput, the platform was refined to accommodate up to four VAM vascular models simultaneously (**Figure 5I**). With a tubing splitter, a single peristaltic pump could perfuse four channels in parallel.

We performed peristaltic pump-driven flow studies on VAM platforms at flow rates of 1 to 15 mL/min for up to three days. The system supports longer-term experiments, when media is periodically replenished (**SI, video S3**). Both straight and sinusoidal vessel geometries were tested and flow rates were adjusted (**Figure 5F, H**). using **Eq. 5-7,** to achieve physiologically relevant shear stresses of 3-50 dyne/cm^2 within the lumens [60].

At flow rates above 5 mL/min, complete elimination of leakage at the needle-model interface was not possible. However, leakage remained minimal and had a negligible influence at low flow rates (<5 mL/min); (**Figure E-G).** At higher flow rates (> 12 mL/min), leakage increased, resulting in greater differences between theoretical and experimental flow rates based on collected fluid volume **(Figure 5G**). Consequently, theoretical and experimental shear stress values differed by approximately 20% at 15 mL/min.

Nonetheless, flow rates around 1 mL/min are sufficient to introduce shear stresses greater than 3 dyne/cm^2, , levels known to promote the formation of functional vascular endothelium [10]. Most perfusion culture studies operate within 0.1–3.0 mL/min, as excessive flow can reduce cell viability [55]. Moreover, our setup can generate high shear stresses (~40 dyne/cm^2), proving its relevance beyond large vein conditions (~1 dyne/cm^2) and enabling modelling of small arteriolar flows where shear stress can reach 50 to 80 dyne/cm^2 [60] (**Figure 5G**).

Although this study focuses on the design and implementation of perfusion platforms customized for geometries of VAM constructs, we acknowledge that direct benchmarking against commercial systems such as AIM Biotech or Kirkstall Quasi Vivo [61, 62] was not performed.

2.8 Precision Control Over the Flow Parameters and Diffusional Permeability

Continuous perfusion of tissue scaffolds necessitates the ability of the scaffold to withstand both hydraulic pressure and fluid shear, and a perfusion platform that allows precise control over these parameters. building on our previous open platform designs (**Figure 5**), we engineered a closed-chamber modular system that accommodates 3D-printed models and enables performance evaluation of the construct-platform assembly under flow conditions (**Figure 6A-C, SI video S4**). Flow rates between 0.3 and 3 mL/min were applied under both uni- and bidirectional conditions, adjustable via a graphical interface (**Figure 6B**).

To our knowledge, this platform uniquely provides simultaneous, precise control of flow within the vascular lumen and around its surrounding environment (**Figure 6C, SI video S4**)**.** Such pressure gradients in the extracellular matrix (ECM) have been found to modulate sprouting angiogenesis [63] and cell migration [13].

Although flow and diffusion control are standard in hydrogel microfluidics, our system integrates these features into freeform, 3D-printed vascular constructs using VAM. This enables non-planar, branched, and tunable geometries that surpass traditional chip-based platforms. The reported diffusion results are specific to the GelMA–PEGDA resin and may vary with other formulations.

Previous studies have indicated that morphological changes in blood vessels occur at shear stresses of approximately 5 dyne/cm^2, corresponding to flow rates of 1-2 mL/min in our systems. These conditions support the formation of a functional vascular barrier with reduced leakage and provide a framework for future cell-embedded VAM constructs, where encapsulated EA.hy926 cells could be used to quantify vascular permeability or analyze cytoskeletal organization under varying flow regimes. [10] .

Unlike traditional shear chambers, our assembled setups employ pulsatile flow, inducing both pulsatile strain and the expansion/contraction of the surrounding hydrogel, making the model sensitive to pressure in addition to shear stress, mimicking the systolic and diastolic pressure dynamics characteristic of physiological blood flow [10].

However, peristaltic pumps can be adapted by incorporating pulsation dampeners to study laminar flow conditions when necessary [64]. Pulsatile flow was achieved by operating the peristaltic pump without the inline pulse dampener, transmitting its inherent cyclic pressure waveform directly to the construct. Previous studies have shown that continuous laminar flows in perfusion culture promote uniform endothelial cell alignment and junction formation. At the same time, pulsatile flow tends to result in more randomized cell organization [64, 65]. In our setup, the Integration of a pressure dampener within the inlet tubing effectively smoothed the flow profile and functioned reliably across 0.3-3 mL/min (**Figure 6D**). The geometries presented in this study are relatively simple (**Figure 6E, SI videos S7 and S8**) and serve as controlled models to validate perfusability, fabrication fidelity, and cell compatibility. We acknowledge that such designs could also be achieved with other techniques, such as sacrificial molding or lithographic patterning. However, the intrinsic ability of VAM to fabricate complex, non-layered, freeform geometries within seconds remains beneficial for rapid prototyping and iterative design.

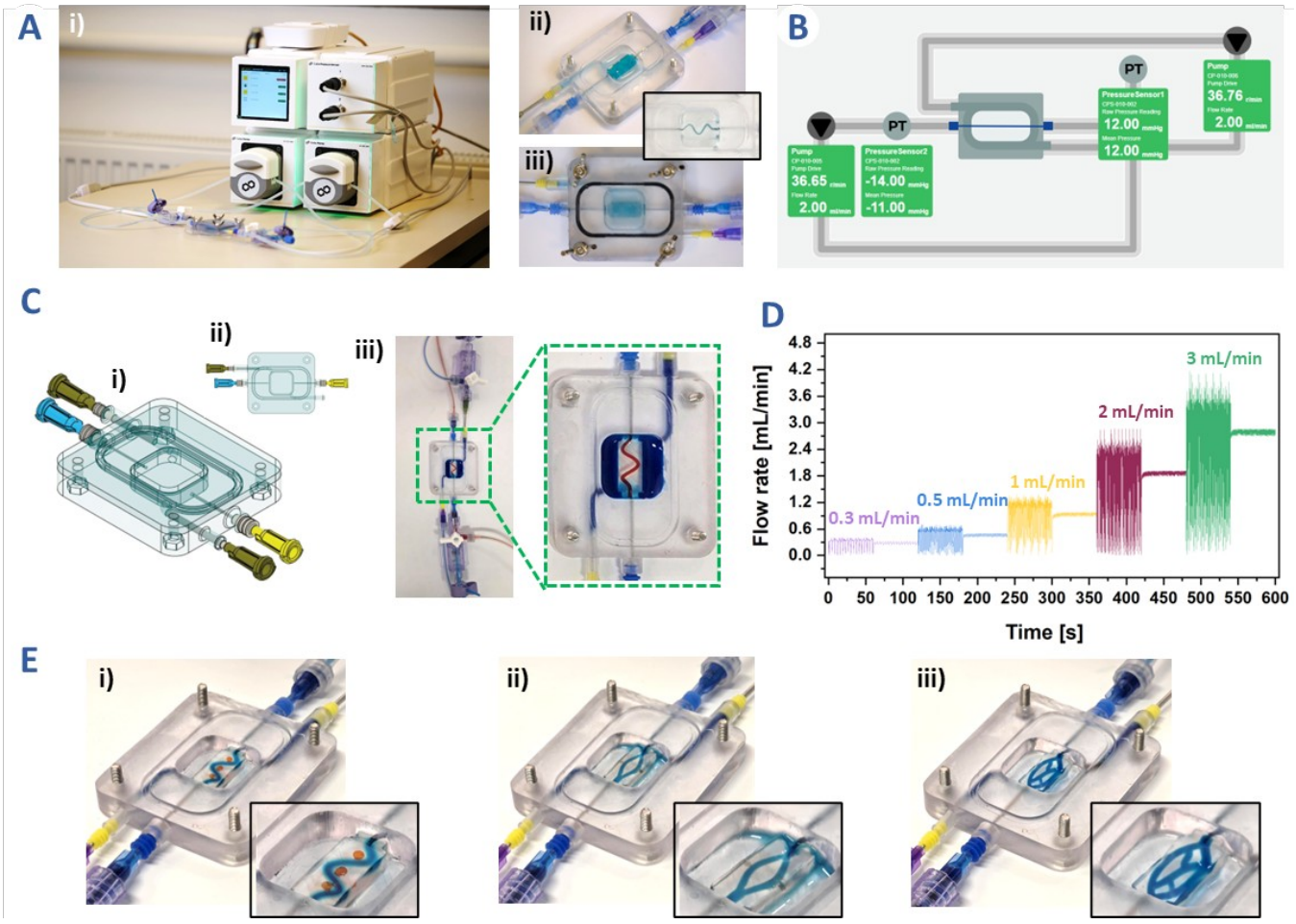

Figure 6 A) *Integrated closed chamber perfusion setup for VAM models testing (i), chamber assembly with VAM model (ii, iii);* ***B)*** *System's graphical interface designed for easy control of fluid flow rate and pressure monitoring;* ***C)*** *Chamber design for VAM model side view (i) and top view (ii). Perfusion experiments carried out within the assembled setup (iii);* ***D)*** *Flow rate measurements for the perfusion system. The set flow rates are plotted in different colors, where the first measurement was carried out without a pulse dampener and the second one with a pulse dampener;* ***E)*** *Perfusion chamber adapted for VAM sample testing with high freedom of model design e.g., sinusoidal (i), branched (ii) or hierarchical vascular-like network designs (iii).*

As a preliminary proof-of-concept, we employed methylene blue dye diffusion to assess the relative permeability of our vascular models [10] (**Figures 7A-B, SI Figure S4, SI Videos S4 and S5**). We observed the dye spread through the channel walls, with approximately 30% diffusion within 30 minutes (**Figure 7B-ii**), eventually covering an area of approximately 1 cm^2 (**Figure 7B-iii**). Although this provided visual and semi-quantitative evidence of solute transport across the hydrogel walls, it does not capture size-selective permeability or precise barrier integrity. This can be more accurately evaluated using molecular tracers, such as FITC-dextran (particularly the 70 kDa variant), which is widely considered the standard for assessing endothelial permeability and paracellular transport in vascularized constructs. Methylene blue was selected here for its strong visible absorbance, low cost, and rapid imaging, making it suitable for proof-of-concept testing.

2.9 Computational Simulations of Flow and Dye Transport

To complement our experimental assessment of perfusion and permeability, we performed computational simulations using COMSOL Multiphysics (**Figure 7C-D**). Transient two-dimensional (2D) simulations were conducted to investigate fluid flow and dye transport dynamics in the printed vascular constructs. The model separately solved the Navier-Stokes equation for laminar flow in the vessel and Brinkman's equation for fluid penetration into the porous hydrogel, assuming negligible hydrogel perfusion compared to intraluminal flow. Following the resolution of the flow field, dye transport into the hydrogel matrix was simulated using the transient advection-diffusion equation. PBS was modeled at 25 °C with a density of 997 kg/m^3 and dynamic viscosity of 0.00089 Pa·s. The hydrogel was treated as a porous medium with a characteristic pore size of 100 nm, corresponding to a permeability of ~1.0 × 10^{-15} m² based on the relation by Cuccia et al. [66]. The porosity (0.6) and dye diffusivity ($6.74 \cdot 10^{-10} m^2/s$) were set to standard values for polymer hydrogels and methylene blue, respectively.

Boundary conditions (**Figure 7C**) included constant inlet velocity for vessel perfusion, zero-gradient outlet conditions, and pressure-matched walls between the vessel and hydrogel. For dye transport, the vessel wall served as a concentration source, with inlet values matching those in the luminal fluid.

Simulations were conducted at three flow rates of 0.3, 1.0, and 3.0 mL/min. All simulated conditions remained within laminar regime (Re < 100). At these flow rates, the experimental leakage is minimal (see **Figure 5E-F**); thus, we neglected the leakage of fluid in the simulations. However, the contribution of leakage should be considered for flow rates above 12 mL/min.

Simulations confirmed the laminar regime and revealed an increasing asymmetry in the velocity distribution at higher flow rates, due to curvature-induced effects (**Figure 7D, SI Figure S5A**). Pressure gradients scaled proportionally with flow rate. Despite this, dye permeation into the hydrogel showed minimal dependence on the flow rate (**Figure 7E, SI, Figure S5B, C, videos S9-11**), consistent with the experimental data (**Figure 7A**). This suggests that dye transport was primarily driven by diffusion rather than convection, with only modest enhancement from advective effects at higher flow rates.

Given that dye diffusion shows minimal dependence on flow rate, both 2D and 3D models are expected to yield comparable results for concentration distributions and transport dynamics. Accordingly, the adoption of a 2D representation is physically justified and computationally efficient [67].

Additionally, we conducted a pilot *in vivo* study using *Galleria mellonella* larvae (**Figure S6A**) to compare active (biological) and passive dye transport, complementing our *in vitro* perfusion findings. Live larvae showed dynamic, non-uniform dye redistribution consistent with active convective transport, while dead larvae exhibited limited diffusion confined to the injection site (**Figure S6B-C**). These results reinforce the importance of perfusion for long-range transport in tissue models; details are provided in SI.

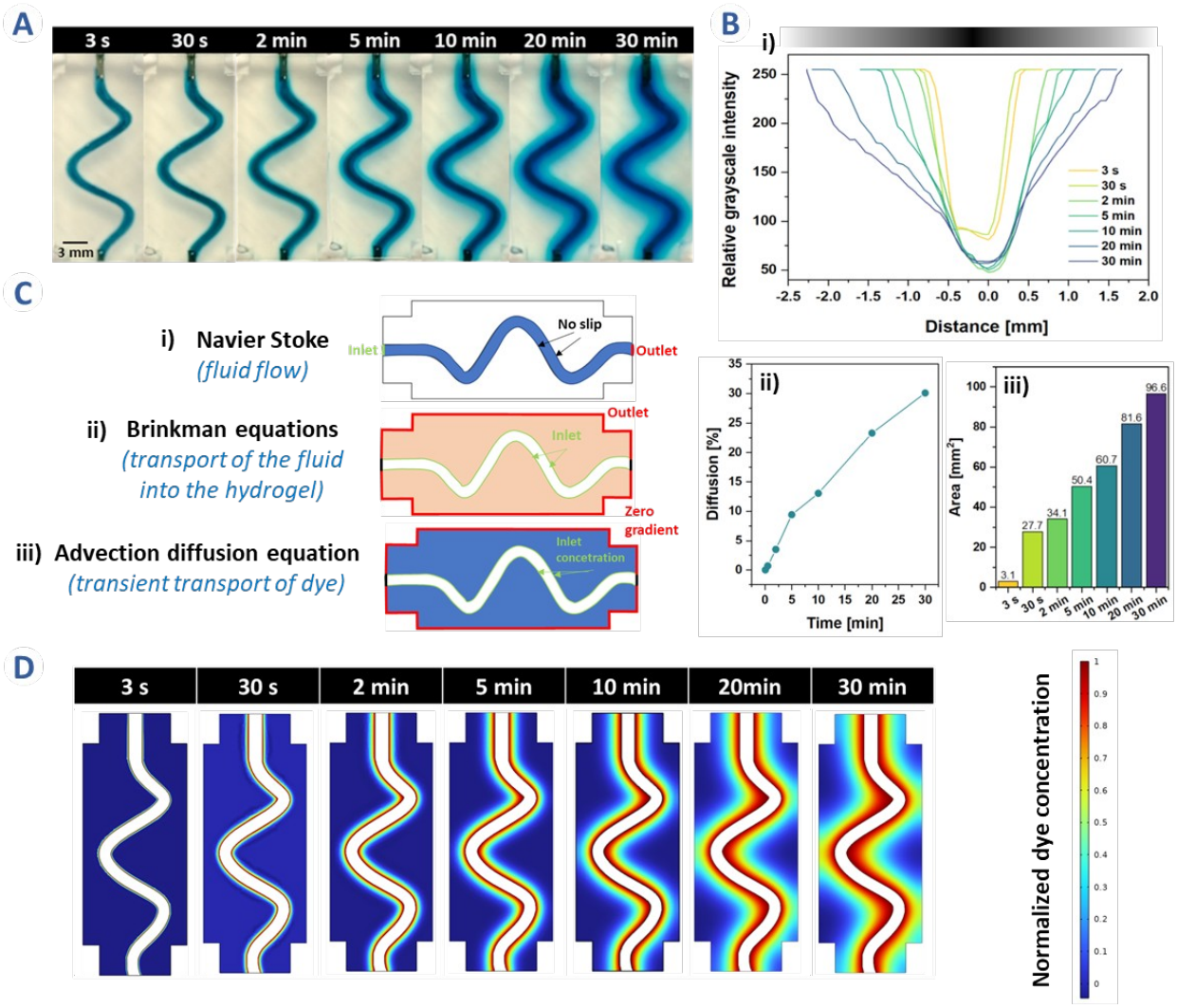

Figure 7 A) *Dye permeation images taken at different perfusion timepoints;* ***B)*** *Dye permeation distance plotted against relative grayscale intensity of the taken image allowing to distinguish higher intensity within the channel and lowering intensities of permeation areas, for the flow rate 1 mL/min (i), Quantified % of diffusion into the channel walls (calculated as percentage intensity) (ii); Increase in the dye coverage area of the sample (iii);* ***C)*** *Geometry and boundary conditions for the different solved problems using computational simulation: (i) In fluid flow analysis, the perfusion comes from the left, with a constant velocity (inlet) to the right (outlet), (ii) To simulate fluid transport inside the hydrogel, the Brinkman's equations are solved, (iii) To simulate dye transport, advection diffusion equations are solved, with the vessel walls as the inlets;* ***D)*** *Relative concentration of dye in the porous medium compared to that in the artificial blood vessel at different time points for fluid flows of (i) 1 mL/min, dimensions of the simulated gel and embedded vessel were taken from the 3D-printed geometry.*

3. Conclusions and Limitations

This study demonstrates the rapid fabrication (<1 minute) of perfusable vascular structures using volumetric additive manufacturing (VAM) and a reusable GelMA–PEGDA resin. The development of recyclable resin introduces a sustainable manufacturing dimension to volumetric bioprinting, minimizing material consumption and promoting greener laboratory practices. To replicate physiological conditions, we developed custom-designed perfusion platforms to provide precise control over flow rate, shear stress, and pressure, key

parameters for simulating physiological conditions. The system supports both pulsatile and laminar flow and is compatible with cell culture.

Experimental dye permeation studies, corroborated by computational simulations, showed that solute transport in the matrix is largely governed by diffusion and is minimally affected by changes in flow rate. Complementary *in vivo* studies in *Galleria mellonella* larvae further indicated that, although diffusion remains the primary transport mechanism, active perfusion can enhance solute movement in a physiological context.

The current work focused primarily on platform validation and material performance. Functional biological responses to flow, such as cytoskeletal alignment, barrier integrity, or gene expression, were not assessed. Only endothelial-like cells were incorporated, which we acknowledge as a limitation. Future work will employ primary endothelial cells to enhance the physiological relevance and translational potential of the platform in vascular tissue engineering and drug screening applications. Finally, although the presented resin formulation offers printability, mechanical stability, and optical clarity, it remains compositionally distinct from native vascular ECM, which is rich in collagen and elastin fibers. Future work will also need to focus on integrating ECM-derived biopolymers to more closely mimic the biochemical cues of native tissue while preserving the high-fidelity printing performance of VAM resins.

4. Experimental section

4.1 Materials and Methods

Gelatin type A (acid-cured, type A, from porcine skin; ~300 g Bloom), phosphate-buffered saline (PBS), Methacrylic anhydride (MAA), polyethylene glycol diacrylate (PEGDA; average Mn 700), lithium phenyl-2,4,6-trimethylbenzoylphosphinate (LAP) with purity ≥ 95%, were purchased from Sigma-Aldrich (St. Louis, MO, USA). Dialysis membrane (Mw cut-off (MWCO): 14 kDa) was obtained from Membra-Cel™, (United States). Dyes: Congo Red and Methylene Blue were purchased from TCI (TCI EUROPE N.V., Zwijndrecht, Belgium), and black particles (Noir Irgalene BGL) were obtained from Ciba-Geigy AG (Switzerland). Methacrylated gelatin was synthesized following our previous protocols [59, 68].

4.2 Resin formulation for VAM

Different resin formulations were prepared by varying the concentrations of GelMA, PEGDA, and the concentration of photoinitiator LAP (0.3 to 1 mg/mL) [42, 69]. The quantities of polymers and photoinitiators are specified in (**SI, Table S1**). For instance, to prepare resin GelMA 5% (w/v), PEGDA 10 % (v/v), LAP 0.3 mg/mL). Stock solutions were prepared as follows: GelMA was dissolved in PBS at a concentration of 7.5% (w/v), and PEGDA was diluted in PBS to a concentration of 30% (w/v). All stock solutions were heated to 37 °C until completely dissolved. To prepare resin for VAM, stock solutions were combined in a 2:1 ratio of GelMA: PEGDA, and lithium phenyl-2,4,6-trimethylbenzoylphosphinate was added to reach a final concentration of 0.3 mg/mL. Finally, the resin was evenly mixed, and if necessary, bubbles were removed in an ultrasonic bath [52].

4.3 Volumetric printing – VAM

Resins were dispensed into cylindrical borosilicate (BK7) glass vials (Ø 15 mm) [26]. Vials were loaded into a commercial volumetric 3D printer (Tomolite, Readily3D, Switzerland; multiwavelength). The samples were thermally gelated at 4°C prior to printing. Models for printing were designed in SolidWorks (St. Waltham, United States) and generated .STL files were loaded into the printer software (Apparite, Readily3D, Switzerland). Prior to printing, the resin's refractive index was measured using a SmartRef (LAB Meister, Anton Paar GmbH, Graz, Austria) and input into the software. Printing was performed with a 405 nm light source. After printing, the vials

were heated to 37°C, and uncured resin was collected. The printed constructs were then washed gently with 37°C PBS [1, 29].

4.4 Characterization

Resolution test

To evaluate the resolution capabilities of the volumetric printing technique, we have designed two models. The first consisted of a star-shaped object with a diagonal 3 mm and a thickness of 1 mm, designed to assess the minimum feature size - fineness (a positive characteristic) achievable with the printing process (**Figure 2G**). The second model was a rectangular block (8 mm width, 4 mm thickness, 15 mm height) with internal channels whose diameters decreased from 1.5 mm to 0.1 mm to determine the minimum printable internal diameter (a negative characteristic) (**Figure 2F**). The models were printed and measured to compare the model and print dimensions.

Rheological properties

Using an Anton Paar MCR 302 rheometer (Anton Paar, Ghent, Belgium), the crosslinking kinetics of the resins were assessed. Time sweep experiments were performed at a frequency of 10 Hz, with 1.0% constant strain at 25°C (n = 3, independent measurements); 15 seconds after the start of the measurement, the light source (Dymax, QX4, VisiCure – 405 nm, intensity: ~14.9 W/cm², Mavom, Kontich, Belgium) was activated for the remaining 105 s. The plate-plate measuring system was used, featuring a 25 mm diameter upper plate and a 100 µm gap size [70, 71]. Samples were *in situ* formed on the rheometer plate with a 1 mm gap at 25 °C before starting measurements.

Temperature sweep: Experiments were performed at a frequency of 1.0 Hz, with a strain rate ranging from 0.1% to 100% strain, starting at 15°C and finishing at 40 °C. The points were recorded every 30 s.

Material opacity

To determine the opacity of the resins, absorbance measurements were carried out using a UV multimode plate reader (Spark, TECAN, Trading AG, Switzerland). To obtain the percentage opacity of a material from its absorbance, **Eq. 1-3** was used [72]:

$$A = \log_{10}\left(\frac{1}{T}\right) \quad (Eq.1)$$

$$\%T = 100 \cdot 10^{-A} \quad (Eq.2)$$

$$\%\,Material\ opacity = 100\,\% - \%T \quad (Eq.3)$$

Where A is absorbance and T is the transmission.

Digital Light processing for rapid prototyping of sample holders and perfusion platforms

Perfusion platforms for securing objects during perfusion were designed in CAD software (SolidWorks, St. Waltham, United States). Lithographic printing was performed using the Asiga MAX ASIGA 27X DLP printer (Erfurt, Germany), equipped with a 405 nm wavelength UV LED light projector. Parts were printed using ABS-Like Resin+ (Shenzhen Anycubic Technology Co., Ltd.), and Asiga Composer software was used to position the CAD models on

the build platform and set parameters (layer thickness of 100 µm, layer exposure time of 10 seconds, and light intensity of 15 mW/cm²). After 3D printing, the parts were washed with isopropanol to remove all resin residues [73].

Microscopic evaluations and sample imaging

Images of the resins and 3D-printed samples were taken using a Fujifilm digital camera (Fujifilm X-H2S). Methylene blue was used to stain the printed constructs, allowing for better visualization of the otherwise transparent hydrogels.

3D printed samples were examined under an inverted microscope (Zeiss Axio Observer, Germany, 5x and 20x objectives) to measure the diameter of printed vessels and assess the finesse of printed structures. We used the coherence contrast mode of the microscope. A minimum of three measurements was taken per sample to calculate average values. Measurements were performed using ZEISS Zen software [29].

Brightfield images during cell culture were taken using a Cell Imager (ZOE, Bio-Rad, Hercules, CA, United States). Fluorescently labeled samples were observed under a ZEISS LSM900 confocal inverted microscope using Airyscan mode (Zeiss, Germany). Micrographs were taken at randomly selected positions to qualitatively assess morphology and distribution of cells [74].

Scanning electron microscope (SEM) images were taken to investigate cell morphology and adhesion for different hydrogel samples (FEI Quanta 200 FEG). For this, cell-seeded scaffolds were fixed with a 2.5% glutaraldehyde solution in cacodylate buffer and subsequently dehydrated with a graded ethanol series (50%, 75%, 90%, and 98%). Samples were air-dried for 3 days, then cross-sectioned and coated with platinum before being observed under SEM [59, 75].

Cell culture and viability assay

The modified endothelial cell line EA.hy926 was maintained in Dulbecco's minimal essential medium (high glucose), supplemented with 10% FBS, 100 µg/mL Penicillin, and 100 U/mL Streptomycin (Thermo Fisher Scientific, Massachusetts, USA), in a humidified CO_2 chamber (37°C, 5% CO2).
To evaluate the hydrogel's biocompatibility and its ability to support cell growth and proliferation, EA.hy926 cells were cultured on hydrogel discs (seeding density: 50,000 cells/cm²) for 1, 3, and 7 days. Cell viability was assessed using the MTS assay (CellTiter 96® Aqueous One Solution Cell Proliferation Assay, Promega, Madison, WI, United States). The samples' absorbance was read at 492 nm using a microplate reader (Epoch, BioTek, United States). EA.hy926 cells viability was calculated over time (1, 3, and 7 days) based on the absorbance values of control wells containing EA.hy926 cells grown in the absence of hydrogel (**Eq. 4**).

$$Viability = \frac{Absorbance\ of\ sample}{Absorbance\ of\ control} \cdot 100\,\% \left(Eq.4 \right)$$

Metabolic activity was measured with a resazurin assay (resazurin sodium salt, Sigma Aldrich, St. Louis, United States) and cell proliferation was evaluated after 1 and 7 d (n = 8) [28].

Channel seeding

After (8-24 h) preincubation, the medium vascular models were removed from the incubator. The medium was aspirated and a 200-µL pipette was used to gently clean the trapped medium out of the channels, filling them with air instead [10]. EA.hy926 cells were dispersed at a seeding density of 2 million/mL, and the channels were

gently filled with 20-25 µL of the cell suspension, ensuring that the air was fully pushed out of the channels. Once the seeding was complete the vascular models were returned to the incubator. After 24-30 h of incubation, non-adherent EA.hy926 cells were removed by gently perfusing the channels with fresh medium. This also helped to remove cell debris from the vascular models [10]. Samples were cultured for one week, with the media refreshed daily.

Cell staining

Cytoskeleton staining (F-actin) was performed with 10 µg/mL Hoechst and 2 µM Alexa Fluor 488 – Phalloidin. To evaluate cellular morphology, EA.hy926 cells were fixed with 4% Paraformaldehyde (PFA), for 30 min, followed by staining with 10 µg/mL Hoechst and 2 µM Alexa Fluor 488 – Phalloidin (ab176753) - Abcam, Cambridge, UK), which was performed in DPBS, 1% BSA at room temperature °C for 90 min. Samples were observed under a ZEISS LSM 900 confocal inverted microscope [59, 68].

Perfusion experiments

For perfusion studies involving a peristaltic pump, VAM channeled structures were positioned on the DLP-printed supporting platforms. The needle tip was carefully inserted and aligned with the lumen of the hydrogel. Silicone tubing (ID = 2 mm, OD = 6 mm) was then connected to the DLP-printed chamber outlet (OD = 2 mm) and the needle tip at the inlet (see **Figure 5D, I**). Tubing was then inserted into a peristaltic pump (Watson-Marlow 323, Watson-Marlow Limited, Cornwall, United Kingdom), enabling flow control by adjusting the RPM (1-300 RPM). Using **Eq. 5** RPM were set to evoke the desired flow rate. Parts were secured in a deep-dish 100-mm Petri dish. Perfusion with PBS either pristine or supplemented with dyes; Congo Red (0.5 mg/mL), Methylene Blue (0.1 mg/mL), or black particles (Noir Irgalene BGL, 0.5 mg/mL) was performed to ease the observation of fluid flow within hydrogel structures.

For the perfusion scale-up experiments, perfusion chambers VAM were adapted to accommodate four samples simultaneously. To divide the fluid flow a channel splitter (RS Components, Corby, United Kingdom) was used. The tubing splitter enables one pump to perfuse four identical channels in parallel, ensuring consistent flow conditions across multiple replicates for comparative testing. A closed chamber perfusion setup was further developed by A4BEE Sp. z o.o. (Wrocław, Poland) to facilitate more accurate testing. The system was integrated with modular cubes to control flow rate and enable pressure readout. A controlled-flow perfusion system was alternatively equipped with fluid pulse dampers (SE-D1606-3NB-PC-316, Darwin Microfluidics, Paris, France) to enable the laminar flow of the medium despite using a peristaltic pump. To validate the flow rate of fluid through the construct, the outlet tubing was connected to a fluid flow sensor evaluation kit (SLF3S-1300F, Sensirion, Stäfa, Switzerland). Tubing adapters were used as needed to ensure a seamless connection of the entire setup.

Flow Rate was calculated using (**Eq. 5**) or directly set on the peristaltic pump. To convert the revolution per minute (RPM) into m^3/s and vice versa, **Eq. 5** was used

$$Q = \frac{RPM \cdot V}{60} (Eq.5)$$

Where $Q \left[\frac{m^3}{s}\right]$ Is the flow rate, RPM, is revolutions per minute, and V [m^3/rev] is the volume per revolution [76].

To determine the flow rate and shear stress, we assumed viscous-dominated flow and PBS as a Newtonian fluid. We further refer to the principle of conservation of momentum for a fluid in a cylinder. Thus, we formulate the

following relationship between the volumetric flow rate and the wall shear stress [10]. The transformed formula (**Eq. 7**) was used to estimate the wall shear stress.

$$Q = \frac{\pi \cdot r^3}{4 \cdot \mu} \cdot \tau \, (Eq.6)$$

$$\tau = \frac{4\,\mu \cdot Q}{\pi \cdot r^3} (Eq.7)$$

where Q $\left[\frac{m^3}{s}\right]$ is the volumetric flow rate, r [m] is the vessel radius, μ is the fluid viscosity (μ_{PBS}= 0.00089 Pa·s), and τ is the shear stress [Pa] at the vessel wall.

Permeability quantification:

Permeability was assessed by recording the perfusion of 10 mg/mL methylene blue dye at a flow rate of 1 mL/min over 30 min through the printed channels. Images were taken at different time points (0-30 min) using a Fujifilm camera (Fujifilm X-H2S). The dye diffusion images were converted into 8-bit, grayscale images (**SI, Figure S4**) with pixel values (0-255) and plotted as a function of dye diffusion distance, over a total length of 4 mm.

The percentage diffusion (as a relative intensity-based diffusion metric) of methylene blue was quantified based on the average fluorescence intensities within the lumen and the channel walls (**Eq. 8**) [77].

$$Diffusion = \frac{Average\ Intensity\,(channel\ walls)}{Average\ Intensity\,(lumen) + Average\ Intensity\,(channel\ walls)} \cdot 100\,\% \, (Eq.8)$$

This metric was used to provide semi-quantitative comparison and does not represent absolute concentration or permeability values. Please note methylene blue does not capture size-selective transport or barrier integrity and was used only as a proof-of-concept tracer.

Numerical Simulations

Computational simulations were performed in COMSOL Multiphysics (COMSOL Inc., Burlington, MA, USA) using a 2D transient model. Separate physics interfaces were used for: (i) laminar flow in the vessel (Navier-Stokes equations), (ii) porous flow in the hydrogel (Brinkman equations), and (iii) dye transport (advection-diffusion). Water was assumed to be the fluid medium with standard physical properties at 25 °C. A hydrogel permeability corresponding to a pore size of 100 nm (~10^{-15} m²) was used, as described by Cuccia et al. [66]. Boundary conditions were assigned as follows: a constant velocity at the inlet, pressure at the outlet, and no-slip at the vessel walls; pressure values at the hydrogel boundaries were inherited from the vessel solution. Dye diffusion simulations assumed inlet concentration matching the dye level inside the lumen. Simulations were carried out for three perfusion rates: 0.3, 1.0, and 3.0 mL/min. The dynamic viscosity of PBS was set to 0.00089 Pa·s at 25°C. Dye diffusivity was set to 6.74 × 10^{-10} m²/s for methylene blue in aqueous media. Mesh sensitivity analysis ensured numerical stability and spatial convergence. Leakage at the inlet–hydrogel interface was not included in the model; this assumption is valid within the investigated flow range (≤3 mL/min), where experimental deviations were minimal. Results were visualized as flow velocity, pressure contours, and normalized dye concentrations, using geometry dimensions derived from the 3D-printed constructs.

Temporal and Segmental Distribution of Methylene Blue in Live and Dead Larvae Model

Final instar larvae of *Galleria mellonella* (Platform for Unique Models Application, Wroclaw Medical University, Poland) weighing 200 ± 20 mg were used. *Galleria mellonella* experiments did not require institutional ethics approval as they are invertebrates. Only healthy, cream-colored individuals with no visible signs of melanization or injury were selected. Larvae were randomly assigned to two experimental groups: live larvae and dead larvae (n=9, each). The latter were euthanized by immersion in liquid nitrogen (- 196 ℃) for 10 seconds and allowed to thaw at room temperature before use. A 1% (w/v) aqueous solution of methylene blue (Biomus, Lublin, Poland) was injected into the proximal section of each larva using a 10 µL Hamilton microsyringe (model 701 RN). To assess the spatial propagation of the dye over time, each larva was divided into three equal-length anatomical segments: proximal (the site of injection), middle, and distal (the farthest from the injection site). Larvae were sampled at 1, 5, and 10 minutes after injection (n = 3 per time point per group). In the live group, individuals were euthanized by immersion in liquid nitrogen at the specified time point to preserve the *in vivo* dye distribution. Larvae in the dead group were injected with dye after thawing, allowing passive diffusion to occur without active circulation or metabolism.

Each larva was manually sectioned with a sterile razor blade into its three predefined segments. Each segment was transferred into 5 mL of ultrapure water and homogenized using a bead mill homogenizer (BeadBug™ 6, Benchmark Scientific, USA) for 2 minutes at 4000 rpm. The resulting homogenates were centrifuged at 12,500 × g for 10 minutes at room temperature. A 100 µL aliquot of the supernatant from each segment was transferred to a 96-well flat-bottom microplate (Sarstedt, Germany), and absorbance was measured at 665 nm using a microplate reader (Multi-scan GO, ThermoFisher Scientific). Control measurements included a blank (ultrapure water only) and a biological control consisting of homogenized larval tissue without methylene blue. Absorbance values were corrected for background by subtracting the mean values of both controls. The extent of dye migration was evaluated by comparing absorbance values across the proximal, medial, and distal segments at each time point. Results were reported as mean ± standard deviation (SD). No statistical analysis was performed due to the pilot nature of the experiment and limited sample size.

4.5 Statistical analysis

All data are reported as mean ± standard deviation (SD), with the number of independent samples (*n*) indicated in the figure captions. All statistical analyses were performed using Origin Pro 2021.

Given the nature of the measurements performed to determine material opacity, data normality was confirmed using the Shapiro-Wilk test, followed by a two-way ANOVA with the Tukey post-hoc test. Similarly, for the comparison of shear stress at different flow rates, data normality was confirmed using the Shapiro-Wilk test, followed by one-way ANOVA with the Tukey post-hoc test.

Given the small sample sizes, non-parametric statistical methods were used to ensure the robustness of the analysis without reliance on normality assumptions. The Kruskal-Wallis test was employed for comparisons between groups in printing resolution tests (positive and negative feature size), followed by Dunn-Sidak's test for post-hoc pairwise comparisons.

The Kruskal-Wallis test was employed for analysis involving minimum printing dose, and G', feature size, area, and perimeter in consecutive printing experiments. In-depth pairwise comparisons were not performed due to limited statistical power.

For cell viability results, the time point was treated as an independent factor. Data normality was confirmed with the Shapiro-Wilk test, followed by one-way ANOVA with the Tukey post-hoc test.

Author Contributions

Conceptualization J.S., A.S., A.J., Data curation J.S., I.B.L., A.T., K.P., Formal Analysis J.S., M.G., K.P., Investigation J.S., M.C., M.G., A.J,. K.P,. Methodology J.S., A.S, M.C., M.G., A.J., K.P., Project administration A.S, Resources A.S, Supervision A.S, E.S., Validation A.S, Visualization J.S., A.T., M.C., Writing – original draft J.S., Writing – review & editing J.S., A.S., K.P., A.J., M.C., M.G, E.S., A.S.

All authors have read and agreed to the published version of the manuscript.

Funding

This study was supported by an Aspirant fellowship from the Fonds National de la Recherche Scientifique de Belgique (FNRS), grant number 46599, 2022, awarded to Julia Siminska-Stanny. Additional support to J.S. was provided by the SofinaBoël Fellowship, the Fondation Philippe Wiener – Maurice Anspach, and the Racquel LeGeros Award (2024) from the European Society for Biomaterials.

Armin Shavandi acknowledges the support of FNRS CDR J.0188.24. Equipment used in this study is financed as a whole or in part by the Walloon Region.

Institutional Review Board Statement

Not applicable.

Informed Consent Statement

Not applicable.

Data Availability Statement

Data supporting the findings of this study are provided in the Supplementary Information. Additional datasets are available from the corresponding author upon reasonable request.

Acknowledgements

The graphical abstract and figure panels 1A, 1C, 1D, 3B, 3I, 4D, 4F, 5A were created with the help of BioRender.com. J.S. gratefully acknowledges the support of a grant from the FNRS (J.S. FNRS-Aspirant, Grant No. FC 46599).

We thank the team of engineers from A4BEE Sp. z o.o. (Wrocław, Poland) for their technical support in the preparation of the microfluidic modules (remotely controlled perfusion chamber with a pressure sensor and two peristaltic pump units), and in particular, we thank Kinga Surmacz and Paweł Godawa for their valuable discussions.

Conflicts of Interest

The authors declare that they have no conflict of interest.

Appendix - Supplementary data

S1.1 - Experimental section

References

1. Bernal, P.N., et al., *Volumetric Bioprinting of Organoids and Optically Tuned Hydrogels to Build Liver-Like Metabolic Biofactories.* Advanced Materials, 2022. **34**(15): p. 2110054.
2. Simińska-Stanny, J., et al., *Hyaluronic Acid Role in Biomaterials Prevascularization.* Advanced Healthcare Materials, 2024. **13**(30): p. 2402045.
3. Iqbal, M.Z., et al., *Breathing new life into tissue engineering: exploring cutting-edge vascularization strategies for skin substitutes.* Angiogenesis, 2024. **27**(4): p. 587–621.
4. Duivenvoorde, L.P.M., et al., *Comparison of gene expression and biotransformation activity of HepaRG cells under static and dynamic culture conditions.* Scientific Reports, 2021. **11**(1): p. 10327.
5. Fukushi, M., et al., *Formation of pressurizable hydrogel-based vascular tissue models by selective gelation in composite PDMS channels.* RSC Advances, 2019. **9**(16): p. 9136–9144.
6. Wang, Y., et al., *Advances in hydrogel-based vascularized tissues for tissue repair and drug screening*. Bioact Mater, 2022. **9**: p. 198–220.
7. Zhang, Y.S., et al., *Bioprinting 3D microfibrous scaffolds for engineering endothelialized myocardium and heart-on-a-chip.* Biomaterials, 2016. **110**: p. 45–59.
8. Song, K.H., et al., *Complex 3D-Printed Microchannels within Cell-Degradable Hydrogels.* Advanced Functional Materials, 2018. **28**(31): p. 1801331.
9. Rapp, J., et al., *2D and 3D in vitro angiogenesis assays highlight different aspects of angiogenesis*. Biochimica et Biophysica Acta (BBA) - Molecular Basis of Disease, 2024. **1870**(3): p. 167028.
10. Polacheck, W.J., et al., *Microfabricated blood vessels for modeling the vascular transport barrier.* Nature Protocols, 2019. **14**(5): p. 1425–1454.
11. Osaki, T., V. Sivathanu, and R.D. Kamm, *Crosstalk between developing vasculature and optogenetically engineered skeletal muscle improves muscle contraction and angiogenesis.* Biomaterials, 2018. **156**: p. 65–76.
12. Linville, R.M., et al., *Physical and Chemical Signals That Promote Vascularization of Capillary-Scale Channels.* Cellular and Molecular Bioengineering, 2016. **9**(1): p. 73–84.

13. Polacheck, W.J., et al., *A non-canonical Notch complex regulates adherens junctions and vascular barrier function*. Nature, 2017. **552**(7684): p. 258–262.
14. Miao, X., et al., *Design, fabrication, and application of bioengineering vascular networks based on microfluidic strategies.* Journal of Materials Chemistry B, 2025.
15. Yeo, M., et al., *Synergistic coupling between 3D bioprinting and vascularization strategies.* Biofabrication, 2023. **16**(1).
16. Moroni, L., et al., *Biofabrication strategies for 3D in vitro models and regenerative medicine.* Nature Reviews Materials, 2018. **3**(5): p. 21–37.
17. Gold, K.A., et al., *3D Bioprinted Multicellular Vascular Models.* Advanced Healthcare Materials, 2021. **10**(21): p. 2101141.
18. Skylar-Scott, M.A., et al., *Biomanufacturing of organ-specific tissues with high cellular density and embedded vascular channels.* Science Advances, 2019. **5**(9): p. eaaw2459.
19. Federici, A.S., et al., *Multicomponent Melt-Electrowritten Vascular Graft to Mimic and Guide Regeneration of Small Diameter Blood Vessels.* Advanced Functional Materials, 2024. **34**(51): p. 2409883.
20. Ma, C., et al., *Photoacoustic imaging of 3D-printed vascular networks.* Biofabrication, 2022. **14**.
21. Simińska-Stanny, J., et al., *Borax - and tannic acid-based post-3D-printing treatment to tune the mechanical properties of scaffolds.* Biomaterials Science, 2025. **13**(13): p. 3689–3706.
22. Fazal, F., et al., *Fabrication of a Compliant Vascular Graft Using Extrusion Printing and Electrospinning Technique.* Advanced Materials Technologies, 2024. **9**(23): p. 2400224.
23. Größbacher, G., et al., *Volumetric Printing Across Melt Electrowritten Scaffolds Fabricates Multi-Material Living Constructs with Tunable Architecture and Mechanics.* Advanced Materials, 2023. **35**(32): p. 2300756.
24. Rizzo, R., et al., *Optimized Photoclick (Bio)Resins for Fast Volumetric Bioprinting.* Advanced Materials, 2021. **33**(49): p. 2102900.
25. Bertana, V. and M. Periolatto, *Volumetric 3D Printing*, in *High Resolution Manufacturing from 2D to 3D/4D Printing: Applications in Engineering and Medicine*, S.L. Marasso and M. Cocuzza, Editors. 2022, Springer International Publishing: Cham. p. 131–151.
26. Delrot, P., *Volumetric 3D printing for Life Science applications*. 2024, Readily3D SA. p. 23.
27. Kelly, B.E., et al., *Volumetric additive manufacturing via tomographic reconstruction.* Science, 2019. **363**(6431): p. 1075–1079.
28. Bernal, P.N., et al., *Volumetric Bioprinting of Complex Living-Tissue Constructs within Seconds.* Advanced Materials, 2019. **31**(42): p. 1904209.
29. Gehlen, J., et al., *Tomographic volumetric bioprinting of heterocellular bone-like tissues in seconds.* Acta Biomaterialia, 2023. **156**: p. 49–60.
30. Riffe, M.B., et al., *Multi-Material Volumetric Additive Manufacturing of Hydrogels using Gelatin as a Sacrificial Network and 3D Suspension Bath.* Advanced Materials, 2024. **36**(34): p. 2309026.
31. Krumins, E., et al., *Glycerol-based sustainably sourced resin for volumetric printing.* Green Chemistry, 2024. **26**(3): p. 1345–1355.
32. Stoecker, L., et al., *Xolography for Biomedical Applications: Dual-Color Light-Sheet Printing of Hydrogels With Local Control Over Shape and Stiffness.* Advanced Materials, 2025. **37**(10): p. 2410292.
33. Viola, M., et al., *Thermal Shrinking of Biopolymeric Hydrogels for High Resolution 3D Printing of Kidney Tubules.* Advanced Functional Materials, 2024. **34**(46): p. 2406098.
34. McQueen, A. and C.M. Warboys, *Mechanosignalling pathways that regulate endothelial barrier function.* Current Opinion in Cell Biology, 2023. **84**: p. 102213.
35. Peterson, L.W. and D. Artis, *Intestinal epithelial cells: regulators of barrier function and immune homeostasis.* Nature Reviews Immunology, 2014. **14**(3): p. 141–153.
36. Wang, D., et al., *Microfluidic bioprinting of tough hydrogel-based vascular conduits for functional blood vessels.* Science Advances. **8**(43): p. eabq6900.
37. Dessalles, C.A., et al., *Integration of substrate- and flow-derived stresses in endothelial cell mechanobiology.* Communications Biology, 2021. **4**(1): p. 764.

38. Fowler, M., et al., *Guiding vascular infiltration through architected GelMA/PEGDA hydrogels: an in vivo study of channel diameter, length, and complexity.* Biomater Sci, 2025. **13**(11): p. 2951–2960.
39. Duan, J., et al., *3D Bioprinted GelMA/PEGDA Hybrid Scaffold for Establishing an In Vitro Model of Melanoma.* J Microbiol Biotechnol, 2022. **32**(4): p. 531–540.
40. Gao, J., et al., *3D-Printed GelMA/PEGDA/F127DA Scaffolds for Bone Regeneration.* J Funct Biomater, 2023. **14**(2).
41. Hall P, C.D., Wheeler T, Ostojich D, Aptecker J, Liashenko I, et al. x. , *A versatile and high-resolution hydrogel platform for volumetric additive manufacturing based on poly(ethylene glycol) diacrylate and alginate blends.* ChemRxiv, 2024.
42. Hall, P., et al., *A versatile and high-resolution hydrogel platform for volumetric additive manufacturing based on poly (ethylene glycol) diacrylate and alginate blends.* Advanced Materials Technologies, 2024.
43. Rodríguez-Pombo, L., et al., *Volumetric 3D printing for rapid production of medicines.* Additive Manufacturing, 2022. **52**: p. 102673.
44. Madrid-Wolff, J., et al., *Controlling Light in Scattering Materials for Volumetric Additive Manufacturing.* Advanced Science, 2022. **9**(22): p. 2105144.
45. Xie, M., et al., *Volumetric additive manufacturing of pristine silk-based (bio)inks.* Nat Commun, 2023. **14**(1): p. 210.
46. Lian, L., et al., *Rapid Volumetric Bioprinting of Decellularized Extracellular Matrix Bioinks.* Advanced Materials, 2024. **36**(34): p. 2304846.
47. Franck, A., *Viscoelasticity and dynamic mechanical testing*, T.I. Germany, Editor.
48. Shie, M.-Y., et al., *Effects of Gelatin Methacrylate Bio-ink Concentration on Mechano-Physical Properties and Human Dermal Fibroblast Behavior.* Polymers, 2020. **12**(9): p. 1930.
49. Zhou, M., et al., *Microbial transglutaminase induced controlled crosslinking of gelatin methacryloyl to tailor rheological properties for 3D printing.* Biofabrication, 2019. **11**: p. 025011.
50. Kavalli, T., *Matériaux photopolymères avancés et systèmes de photo-amorçages pour l'impression 3D*. 2019.
51. Simińska-Stanny, J., et al., *Geometrical Designs in Volumetric Bioprinting to Study Cellular Behaviors in Engineered Constructs.* Advanced Healthcare Materials, 2026. **15**(6): p. e03550.
52. Simińska-Stanny, J., et al., *Geometrical Designs in Volumetric Bioprinting to Study Cellular Behaviors in Engineered Constructs.* bioRxiv, 2025: p. 2025.07.14.664683.
53. Ghosh, R.N., et al., *An insight into synthesis, properties and applications of gelatin methacryloyl hydrogel for 3D bioprinting.* Materials Advances, 2023. **4**(22): p. 5496–5529.
54. Hutson, C.B., et al., *Synthesis and characterization of tunable poly(ethylene glycol): gelatin methacrylate composite hydrogels.* Tissue Eng Part A, 2011. **17**(13-14): p. 1713–23.
55. Beris, A.N., et al., *Recent advances in blood rheology: a review.* Soft Matter, 2021. **17**(47): p. 10591–10613.
56. Goy, C.B., R.E. Chaile, and R.E. Madrid, *Microfluidics and hydrogel: A powerful combination.* Reactive and Functional Polymers, 2019. **145**: p. 104314.
57. Weigel, N., et al., *From microfluidics to hierarchical hydrogel materials.* Current Opinion in Colloid & Interface Science, 2023. **64**: p. 101673.
58. Xie, R., et al., *Engineering of Hydrogel Materials with Perfusable Microchannels for Building Vascularized Tissues.* Small, 2020. **16**(15): p. 1902838.
59. Simińska-Stanny, J., et al., *Advanced PEG-tyramine biomaterial ink for precision engineering of perfusable and flexible small-diameter vascular constructs via coaxial printing.* Bioact Mater, 2024. **36**: p. 168–184.
60. Ballermann, B.J., et al., *Shear stress and the endothelium.* Kidney International, 1998. **54**: p. S100–S108.
61. Walji, N., S. Kheiri, and E. Young, *Angiogenic Sprouting Dynamics Mediated by Endothelial-Fibroblast Interactions in Microfluidic Systems.* Advanced Biology, 2021. **5**.
62. Miranda Azpiazu, P., et al., *A novel dynamic multicellular co-culture system for studying individual blood-brain barrier cell types in brain diseases and cytotoxicity testing.* Scientific Reports, 2018. **8**.

63. Galie, P.A., et al., *Fluid shear stress threshold regulates angiogenic sprouting*. Proceedings of the National Academy of Sciences, 2014. **111**(22): p. 7968–7973.
64. Abello, J., et al., *Peristaltic pumps adapted for laminar flow experiments enhance in vitro modeling of vascular cell behavior*. Journal of Biological Chemistry, 2022. **298**(10): p. 102404.
65. Morimoto, Y., et al., *Microfluidic system for applying shear flow to endothelial cells on culture insert with collagen vitrigel membrane*. Sensors and Actuators B: Chemical, 2021. **348**: p. 130675.
66. Cuccia, N.L., et al., *Pore-size dependence and slow relaxation of hydrogel friction on smooth surfaces*. Proceedings of the National Academy of Sciences, 2020. **117**(21): p. 11247–11256.
67. Bashir, S., J.M. Rees, and W.B. Zimmerman, *Simulations of microfluidic droplet formation using the two-phase level set method*. Chemical Engineering Science, 2011. **66**(20): p. 4733–4741.
68. Simińska-Stanny, J., et al., *Optimizing phenol-modified hyaluronic acid for designing shape-maintaining biofabricated hydrogel scaffolds in soft tissue engineering*. Int J Biol Macromol, 2023. **244**: p. 125201.
69. Madrid-Wolff, J., et al., *A review of materials used in tomographic volumetric additive manufacturing*. MRS Communications, 2023. **13**(5): p. 764–785.
70. Hapipi, N.M., et al., *The Rheological Studies on Poly(vinyl) Alcohol-Based Hydrogel Magnetorheological Plastomer*. Polymers, 2020. **12**(10): p. 2332.
71. Falandt, M., et al., *Hybrid supramolecular-covalent bioresin promotes cell migration and self-assembly in light-based volumetric bioprinted constructs*. BioRxiv, 2025.
72. Hospodiuk-Karwowski, M., et al., *Dual-charge bacterial cellulose as a potential 3D printable material for soft tissue engineering*. Composites Part B: Engineering, 2022. **231**: p. 109598.
73. Komissarenko, D., et al., *DLP 3D printing of high strength semi-translucent zirconia ceramics with relatively low-loaded UV-curable formulations*. Ceramics International, 2023. **49**(12): p. 21008–21016.
74. Simińska-Stanny, J., et al., *Optimizing phenol-modified hyaluronic acid for designing shape-maintaining biofabricated hydrogel scaffolds in soft tissue engineering*. International Journal of Biological Macromolecules, 2023. **244**.
75. Shavandi, A., et al., *Biomaterial ink based on bacterial polyglucuronic acid for tissue engineering applications*. Next Materials, 2024. **4**: p. 100181.
76. Schneider, S., et al., *Peristaltic on-chip pump for tunable media circulation and whole blood perfusion in PDMS-free organ-on-chip and Organ-Disc systems*. Lab on a Chip, 2021. **21**(20): p. 3963–3978.
77. Cai, B., et al., *One-step bioprinting of endothelialized, self-supporting arterial and venous networks*. Biofabrication, 2025. **17**(2).